International Journal of Heat and Mass Transfer 156 (2020) 119915

Contents lists available at ScienceDirect

International Journal of Heat and Mass Transfer

journal homepage: www.elsevier.com/locate/hmt

Phase-field modeling of macroscopic freezing dynamics in a cylindrical vessel

Ji-Qin Li, Tai-Hsi Fan*

Department of Mechanical Engineering, University of Connecticut, Storrs, CT 06269, USA

ARTICLE INFO

Article history:
Received 6 November 2019
Revised 29 April 2020
Accepted 3 May 2020
Available online 12 May 2020

Keywords:
Phase-field model
Freezing dynamics
Freeze concentration
Phase transition
Protein pharmaceuticals
Supercooled water

ABSTRACT

Freezing is an essential step in pharmaceutical manufacturing processes for a long-term storage of therapeutic proteins. However, the process itself may affect the stability of proteins. Better understanding and quantification of freezing dynamics and the local environment from liquid solution to the frozen state would help to mitigate negative impacts on the protein products during freezing and subsequent manufacturing processes. We present a phase-field approach to resolve the relevant macroscopic transport phenomena including multi-phase flow, heat transfer, phase transition, and freeze concentration effects coupled with interfacial evolution in a cylindrical vessel. The theoretical formulation and modeling results show good agreement with experimental data.

1. Introduction

Degradation of therapeutic proteins can be of high risk upon administration, and thus protein stability is often a great concern in manufacturing high-quality and high-valued pharmaceutical products. Solutions of therapeutic proteins are often frozen to prevent degradation for a long-term storage. However, freezing process itself is accompanying by protein degradation, possibly owing to ice crystal formation, low temperature, protein-protein interactions and aggregation at a higher concentration, changes of pH and concentration of excipients, and possibly adsorption of proteins on the ice/freeze-concentrate interfaces [1–5]. Similar to most solidification processes, the nucleation and freezing step very much determines the microstructure of ice crystals, distribution of freeze concentrate among ice crystals, and the overall texture of the frozen products. For protein biopharmaceutical solutions, studies have shown that the microstructure of the frozen state is correlated with protein stability [6–9], and has impact on the subsequent processes including the efficiencies of primary and secondary drying, reconstitution, as well as mechanical properties of the dried products [10–13].

Freezing of aqueous solutions involves phase transition from liquid water to ice, which spans multiple spatial and temporal scales starting from precipitation, nucleation and growth, dendrite formation, to the growth and interaction of ice crystals. The process is often coupled with heat, mass, interfacial and momentum transport in the solutions, and further complicated by the change of equilibrium conditions such as freezing point depression as solute concentration increases, and nonequilibrium interfacial kinetics at higher freezing rate. Furthermore, the relevant physicochemical and transport properties are likely temperature-and/or concentration-dependent, including thermal conductivity, solute diffusivity, fluid viscosity, density, latent heat, and specific heats. A few experimental [14–18] and mesoscale theoretical analyses [19,20] have demonstrated the microstructure evolution and the composition of protein and sucrose (as a cryoprotectant) solutions in a frozen state along with freeze concentration of proteins and excipients due to solute exclusion from ice and local transport behaviors. Macroscopic analyses that focus on simplified heat transfer and phase transition behaviors have shown good agreements with experimental observations [21,22]. The semi-empirical models with ice nucleation taken into account was developed for the prediction of average crystal size [23–25]. A relatively complete quantitative investigations on freezing of protein solutions was provided by Nakagawa et al. [24], including empirical estimation of crystal size under various nucleation temperature and cooling rates, local temperature profiles, and the displacement of solidification front in a cylindrical vessel under slow to fast cooling conditions. Roessl et al. [26] have combined fluid dynamics with heat and mass transfer to simulate the temperature distribution and the macroscopic freeze concentration during the freezing process. Nevertheless, still many subtle details in the freezing dynamics are not yet well understood and theoretically quantified.

---

* Corresponding author.
E-mail address: thfan@engr.uconn.edu (T.-H. Fan).

https://doi.org/10.1016/j.ijheatmasstransfer.2020.119915

Nomenclature

$\dot{\boldsymbol{q}}$	heat flux
$\mathcal{D}$	solute diffusivity
$\mathcal{D}^{\infty}$	accommodation factor for solute diffusivity at interface
$\mathcal{S}$	entropy functional
$\boldsymbol{v}_i^{\infty}$	sedimentation velocity of solutes
$\mathbf{g}$	gravity acceleration
$\mathbf{J}_s$	entropy flux
$\boldsymbol{v}$	velocity field
b	position of moving interface in 1D approximation
c_p	specific heat
d	hydrodynamic diameter of solute molecules
e	specific internal energy
f	specific free energy
H	height of the solution
h	heat transfer coefficient
$h_{s\ell}$	coefficient of energy barrier
k	thermal conductivity
l_1	thickness of cover lid
l_2	thickness of stagnant air layer on top of solution
l_3	thickness of vessel wall
l_4	thickness of stagnant air layer beneath the vessel
L_a	latent heat of solid-liquid phase transition
M	interfacial mobility
N	solute-to-water ratio of molar volume
n	total number of solutes
P	interpolation function between solid and liquid phases
p	pressure
R	gas constant
r	radial coordinate
R_i	inner radius of the vessel
R_o	outer radius of the vessel
s	specific entropy
T	temperature
t	time
T_0	freezing temperature of a pure water
U	characteristic velocity
v_n	magnitude of normal-to-interface velocity
$W_{s\ell}$	interfacial thickness
z	axial coordinate

Dimensionless numbers

Λ_sed	sedimentation number
$\Lambda_{s\ell}$	phase-change number
$\mathcal{B}_\text{i}$	Biot number
$\mathcal{C}_\text{h}$	Cahn-Hilliard number
$\mathcal{G}_\text{r}$	local Grashof number
$\mathcal{L}_\text{e}$	Lewis number
$\mathcal{N}_\text{u}$	Nusselt number
$\mathcal{P}_\text{e}$	Peclet number
$\mathcal{P}_\text{r}$	Prandtl number
$\mathcal{R}_\text{a}$	Rayleigh number
$\mathcal{R}_\text{e}$	Reynolds number
$\mathcal{S}_\text{te1}$, $\mathcal{S}_\text{te2}$	Stefan number

Greek symbols

α	thermal diffusivity
β_1, β_2	adjustable factors for solute diffusivity at interface
$\boldsymbol{\omega}$	vorticity field
$\boldsymbol{\sigma}$	viscous stress
χ	Flory's interaction parameter
$\dot{\Gamma}$	entropy production rate
η	dynamic viscosity
$\gamma_{s\ell}$	interfacial energy at solid-liquid interface
Ω	computational domain
ω	vorticity in azimuthal direction
ϕ	phase field variable
ψ	stream function
ρ	mass density
τ	characteristic time
θ	azimuthal direction
ξ	gradient coefficient used in entropy functional
ζ	immobilized coordinate

Subscripts

1	sucrose
2	dilute protein
ℓ	liquid phase
c	solute diffusion
i	solute species
s	solid phase
$s\ell$	solid-liquid phase transition
0	reference property
air	air phase
conv	convection
env	environment
eq	equilibrium
ini	initial condition
inter	interface
sed	sedimentation
side	circumferential wall of the vessel
steel	steel material
T	thermal effect
top	top surface of the computational domain
vis	viscous effect

In principle one can better design and control the cooling conditions, temperature distribution, solute uniformity, and desirable microstructure if the process dynamics can be computationally resolved and optimised. However, the development of high-fidelity computational model is only at the beginning stage due to many challenges encountered from protein-protein and protein-interface interactions to local and bulk solution behaviors, calibrations of thermophysical properties in the supercooled regime, and the computational cost. Recently we have resolved the multiphase transport and interfacial dynamics of freezing process and freeze concentration at the mesoscale along with growth of ice crystals in sucrose solutions [19]. The freeze concentration effect has been integrated to the transient dynamics and topological change of the ice crystals. However, similar analysis at the macroscopic level faces a new challenge because freeze concentration or solute segregation is intrinsically a small-scale phenomena, very difficult to be extended for the prediction of macroscopic behaviors in a vial or vessel. Here we propose a new coarse-grained approach to resolve bulk phase transition, concentration polarization, heat and multicomponent mass transfer, thermophysical properties, bulk fluid flow, convective and gravity effect using the phase-field method without considering the dynamics of individual ice crystals. The computational results are side-by-side compared with the most complete experimental data [15] according to the cylindrical vessel configuration and estimated heat transfer boundary conditions. Without explicit interface tracking, this approach is convenient in resolving the moving boundary with complicated morphological change during phase transition that possibly involves merging or splitting of interfaces. The phase-field variables or order parameters are uniform in homogeneous bulk phases, yet having a narrow and smooth transition across the interface between phases. A rigorous definition of the interfacial thickness is connected with interfacial energy and mobility, which can be proved asymptotically consistent with classical transport model with a sharp interface [27]. Here our theoretical derivation for the non-isothermal process follows entropy analysis in nonequilibrium thermodynamics, and the system dynamics is driven by the increase of entropy with gradient effect due to spatial variation of the assumed phase-field variables [28–31]. The method has been widely developed for mesoscale simulations of solidification process particularly for dendritic pattern formation in pure and alloy systems [32–41]. The theoretical framework has also been expanded for a variety of applications such as in metallic additive manufacturing processes [42,43], and recently be adapted and modified for the analysis of freezing dynamics in sucrose solutions [19,20].

2. Theoretical analysis

Fig. 1 shows the schematic view the problem in hand. The cylindrical vessel has roughly three cooling surfaces from top, bottom, and circumferential walls (Fig. 1). The initial condition is a well-mixed aqueous solution of sucrose excipient as the primary solute and proteins as a secondary component stored in a cylinder vessel. The process starts from 10 °C to a supercooled liquid state with an assumed precipitating temperature. A typical growth of ice phase begins from the wall boundary and progresses toward the center portion of the vessel. The following assumptions are made to simplify the theoretical analysis and computation: (i) thermal radiation and irradiation effects are neglected, (ii) thermal expansion, elasticity and thermal stress of the ice phase are neglected, (iii) density variation across ice/liquid water interface is neglected, and (iv) molecular events such as protein-protein and protein-excipient interactions, and adsorption of proteins on ice/freeze-concentrate interfaces are not considered. The configuration (Fig. 1) follows the experimental setting provided by Rodrigues el al. [15].

2.1. General formulation based on phase-field approach

Because heat transport and local temperature distribution play an important role in this multiphase moving boundary problem, a thermodynamically consistent phase-field formulation is considered to resolve the macroscopic dynamics in a cylindrical coordinate system. The phase-field variables involved in our model are: (i) phase field $\phi_{s\ell}(r, z, t)$ as a non-conserved order parameter that describes phase transition dynamics and distinguishes liquid phase ($\phi_{s\ell} = -1$) from the ice or solid phase ($\phi_{s\ell} = 1$), with r and z indicating local position along the radial and axial coordinates respectively on a cross-sectional plane, and t is time, (ii) ϕ_i for the volume fraction of species dissolved in the solutions, including sucrose as the primary component ($i = 1$) and dilute proteins or excipients ($i = 2, 3, \dots, n$). Following phase-field approach based on irreversible thermodynamic principles [30,31,38], the entropy functional in the material volume can be formulated as

$$\mathcal{S} = \int_\Omega \left\{ \rho s(e, \phi_{s\ell}, \phi_1, \phi_2, \dots, \phi_n) - \frac{1}{2}\xi_{s\ell}^2 |\nabla\phi_{s\ell}|^2 - \sum_{i=1}^{n}\left[\frac{1}{2}\xi_i^2|\nabla\phi_i|^2\right]\right\} dV, \tag{1}$$

where ρ is mass density, s is specific entropy as a function of specific internal energy e and other phase-field variables, n is the total number of solutes to be traced, and coefficients $\xi_{s\ell}$ and ξ_i are assumed constant coefficients for the gradient effects. The first term of the integral indicates the contribution of the entropy density in the bulk phase, the 2nd term represents spatial variation of the phase field for the non-local or gradient effects across solid and liquid phases, and the last term sums up the gradient contributions of species concentrations.

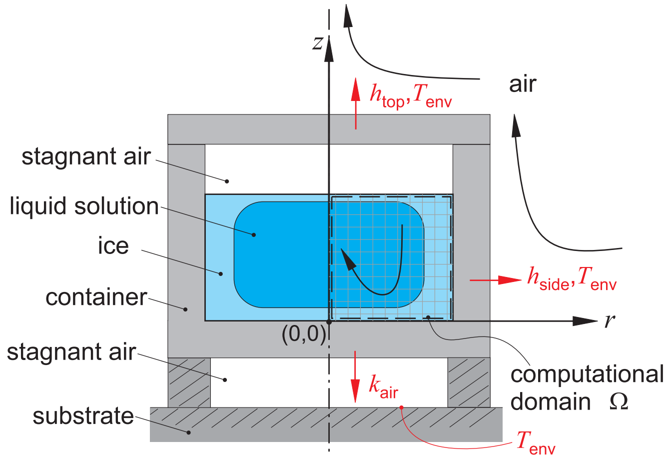

Fig. 1. Schematic of freezing process in a cylindrical vessel. The container is made of steel.

Applying the Reynolds transport theorem to the entropy functional, the entropy transport equation can be generalized as

$$\rho\frac{\mathrm{D}s}{\mathrm{D}t} - \frac{1}{2}\xi_{s\ell}^2\frac{\mathrm{D}}{\mathrm{D}t}|\nabla\phi_{s\ell}|^2 - \sum_{i=1}^{n}\frac{1}{2}\xi_i^2\frac{\mathrm{D}}{\mathrm{D}t}|\nabla\phi_i|^2 = -\nabla\cdot\mathbf{J}_s + \dot{\Gamma}, \tag{2}$$

where $\mathrm{D}/\mathrm{D}t \equiv \partial/\partial t + \boldsymbol{v}\cdot\nabla$ indicates material derivative, $\boldsymbol{v}$ is velocity, $\mathbf{J}_s$ is entropy flux, and $\dot{\Gamma}$ represents local entropy production rate. Considering the relationship between entropy and internal energy, $e = e(s, \phi_{s\ell}, \phi_1, \phi_2, \dots, \phi_n)$, one can express the change of energy as

$$de = Tds + \frac{\partial e}{\partial\phi_{s\ell}}d\phi_{s\ell} + \sum_{i=1}^{n}\frac{\partial e}{\partial\phi_i}d\phi_i, \tag{3}$$

where T is temperature. Thus, the material derivative of entropy in Eq. (2) becomes

$$\frac{\mathrm{D}s}{\mathrm{D}t} = \frac{1}{T}\frac{\mathrm{D}e}{\mathrm{D}t} - \frac{1}{T}\frac{\partial e}{\partial\phi_{s\ell}}\frac{\mathrm{D}\phi_{s\ell}}{\mathrm{D}t} - \sum_{i=1}^{n}\frac{1}{T}\frac{\partial e}{\partial\phi_i}\frac{\mathrm{D}\phi_i}{\mathrm{D}t}. \tag{4}$$

Now, by substituting Eq. (4) into (2) and rearranging the heat flux term in the energy equation as

$$\frac{\rho}{T}\frac{\mathrm{D}e}{\mathrm{D}t} = -\frac{1}{T}\nabla\cdot\dot{\boldsymbol{q}} = -\nabla\cdot\left(\frac{\dot{\boldsymbol{q}}}{T}\right) + \dot{\boldsymbol{q}}\cdot\nabla\left(\frac{1}{T}\right), \tag{5}$$

the entropy production rate in Eq. (2) can be obtained and expressed as

$$\begin{aligned}\dot{\Gamma} &= \dot{\boldsymbol{q}}\cdot\nabla\left(\frac{1}{T}\right) + \left[\xi_{s\ell}^2\nabla^2\phi_{s\ell} - \frac{\rho}{T}\frac{\partial e}{\partial\phi_{s\ell}}\right]\frac{\mathrm{D}\phi_{s\ell}}{\mathrm{D}t} \\ &\quad + \sum_{i=1}^{n}\left[\xi_i^2\nabla^2\phi_i - \frac{\rho}{T}\frac{\partial e}{\partial\phi_i}\right]\frac{\mathrm{D}\phi_i}{\mathrm{D}t} \geq 0,\end{aligned} \tag{6}$$

where the viscous dissipation and capillary work have been neglected due to relatively small dissipation energy. To accommodate the second law of thermodynamics with a positive-definite entropy production rate, the transport equations that describe non-isothermal multiphase dynamics including melting and freezing processes can be developed, and here the corresponding phase-field equations are formulated as

$$\frac{\mathrm{D}\phi_{s\ell}}{\mathrm{D}t} = M_{s\ell}\left[\xi_{s\ell}^2\nabla^2\phi_{s\ell} - \frac{\rho}{T}\frac{\partial e}{\partial\phi_{s\ell}}\right], \tag{7}$$

and

$$\frac{\mathrm{D}\phi_i}{\mathrm{D}t} = \nabla \cdot \left[M_i \nabla \left(\frac{\rho}{T} \frac{\partial e}{\partial \phi_i} - \xi_i^2 \nabla^2 \phi_i \right) \right] \quad \text{for} \quad i = 1, \ldots, n, \tag{8}$$

where interfacial mobility coefficients $M_{s\ell}$ and M_i are assumed positive values. Eq. (7) is non-conservative (Allan-Cahn model), describing the evolution of interfaces for the growth of ice phase, whereas Eq. (8) is conservative (Cahn-Hilliard model) for determining species concentrations. Consider Fourier's law on conduction heat flux, $\dot{\boldsymbol{q}} = -k\nabla T$, where $k \simeq k(T, \phi_{s\ell}, \phi_1)$ is the thermal conductivity, the classical energy equitation is

$$\rho \frac{\mathrm{D}e}{\mathrm{D}t} = \nabla \cdot (k \nabla T). \tag{9}$$

2.2. Continuity and momentum equations

During the freezing process, the fluid flow is driven by gravity effect due to density variation within the flow field. The locally concentrated solution has higher density than the surrounding fluid, and naturally tends to sediment to lower portion of the vessel. This effect is estimated by the Boussinesq approximation. The density ρ that takes phase transition and solute concentration effect into account can be formulated as

$$\begin{aligned} &\rho(T, \phi_{s\ell}, \phi_1, \phi_2, \ldots, \phi_n) = \rho_0 \tilde{\rho} \\ &\simeq \rho_0 \left\{ \textstyle\sum_{i=1}^n \phi_i \tilde{\rho}_i + (1 - \sum_{i=1}^n \phi_i) \left[P \tilde{\rho}_\ell(T, \phi_i) + (1 - P) \tilde{\rho}_s(T) \right] \right\}, \end{aligned} \tag{10}$$

where the scaled density of ice $\tilde{\rho}_s$ and water $\tilde{\rho}_\ell$ are temperature dependent, the reference density ρ_0 is defined as $\rho_\ell(\phi_i \to 0, T \to T_0)$ with T_0 indicating equilibrium freezing temperature of a pure water, and $P = P(\phi_{s\ell})$ is an interpolation function from the liquid ($P = 1, \phi_{s\ell} = -1$) to solid ($P = 0, \phi_{s\ell} = 1$) phases, defined later on by Eq. (20). In this study, we consider all properties are ϕ_1 (sucrose) dependent, but can be further extended to include multi-component effect.

The system is quasi-incompressible in all phases with neglected density variation at the interfaces. The fluid flow continuity equation is

$$\nabla \cdot \boldsymbol{v} = 0. \tag{11}$$

The Navier-Stokes momentum equation with Boussinesq approximation for the buoyant effect is given by

$$\rho \left(\frac{\partial \boldsymbol{v}}{\partial t} + \boldsymbol{v} \cdot \nabla \boldsymbol{v} \right) = -\nabla p + \nabla \cdot \boldsymbol{\sigma} + (\rho - \rho_0)\mathbf{g}, \tag{12}$$

where $\mathbf{g}$ is gravity acceleration, p is pressure, and the viscous stress $\boldsymbol{\sigma}$ for the assumed Newtonian fluid is given by

$$\boldsymbol{\sigma} = \eta \left(\nabla \boldsymbol{v} + \nabla \boldsymbol{v}^{\mathrm{T}} \right), \tag{13}$$

where the dynamic viscosity η across phases can be defined as

$$\eta \simeq \eta(T, \phi_{s\ell}, \phi_1) = \eta_0 \tilde{\eta} \simeq \eta_0 \left[P \tilde{\eta}_\ell(T, \phi_1) + (1 - P) \tilde{\eta}_s \right], \tag{14}$$

with an assumed constant viscosity for the crystal phase $\tilde{\eta}_s \gg \tilde{\eta}_\ell$ and a reference value $\eta_0 = \eta_\ell(\phi_1 \to 0, T \to T_0)$.

Furthermore, in a 3D axisymmetric system with coordinates in radial (r), axial (z), and azimuthal (θ) directions, the momentum equation can be solved by the vorticity-stream function method. By taking curl of the above momentum equation, the vorticity equation can be formulated as

$$\begin{aligned} \rho \frac{\mathrm{D}\boldsymbol{\omega}}{\mathrm{D}t} &= \eta \nabla^2 \boldsymbol{\omega} + \nabla \eta \times \nabla^2 \boldsymbol{v} + \nabla \times \left[\nabla \eta \cdot \left(\nabla \boldsymbol{v} + \nabla \boldsymbol{v}^{\mathrm{T}} \right) \right] \\ &\quad + \nabla \times [(\rho - \rho_0)\mathbf{g}], \end{aligned} \tag{15}$$

where $\boldsymbol{\omega} = (\omega_r, \omega_z, \omega_\theta) = (0, 0, \omega)$ is the vorticity field with non-zero value appears in the azimuthal direction, which is perpendicular to the axisymmetric velocity field. Here the corresponding stream function ψ in the cylindrical coordinate system is defined as

$$\boldsymbol{v} = \left(-\frac{1}{r} \frac{\partial \psi}{\partial z}, \ \frac{1}{r} \frac{\partial \psi}{\partial r}, \ 0 \right). \tag{16}$$

Considering vorticity $\boldsymbol{\omega} = \nabla \times \boldsymbol{v}$, the stream function equation reduces to

$$\frac{\partial^2 \psi}{\partial z^2} + \frac{\partial^2 \psi}{\partial r^2} - \frac{1}{r} \frac{\partial \psi}{\partial r} = -\omega r. \tag{17}$$

The flow field is established by solving the above vorticity and stream function equations in a cylindrical coordinate system.

2.3. Energy equation

The specific internal energy of this multi-component system can be approximated by

$$e(T, \phi_{s\ell}, \phi_1, \phi_2, \ldots, \phi_n) = e_{s\ell}(T, \phi_{s\ell}) + \sum_{i=1}^n RT \langle \chi_i \rangle \phi_i (1 - \phi_i), \tag{18}$$

where $e_{s\ell}$ represents the internal energy of water in both solid to liquid phases, R is gas constant, and $\langle \chi_i \rangle = \langle \chi_i(\phi_{s\ell}) \rangle$ is an apparent or coarse-grained Flory's interaction parameter for a regular solution. The summation term in the internal energy indicates the increase of internal energy due to mixing of ice or liquid water with solutes. At the macroscopic level, the $\langle \chi_i \rangle$ value is a phenomenological parameter that controls the partition effect in an average sense. To accommodate the phase transition, the internal energy $e_{s\ell}$ as a smooth function across ice and liquid water can be expressed as

$$\begin{aligned} e_{s\ell}(T, \phi_{s\ell}) &= e_s(T) + P(\phi_{s\ell}) L_a \\ &= e_\ell(T) + [P(\phi_{s\ell}) - 1] L_a, \end{aligned} \tag{19}$$

where the subscript s and ℓ indicate homogeneous solid and liquid phases, respectively, L_a is the latent heat of solid-liquid phase transition based on the reference equilibrium freezing temperature of pure water T_0. Here we assume that the latent heat is independent of temperature for a small shift of freezing temperature due to freezing point depression. And $P(\phi_{s\ell})$ is an interpolation function for a smooth transition of internal energy from the liquid to solid phases [31], indicated as a dash line in Fig. 2. Here the P function is a 5th-order polynomial that satisfies $P' = P'' = 0$ at $\phi_{s\ell} = \pm 1$, expressed as

$$P(\phi_{s\ell}) = \frac{1}{2} - \frac{15}{16} \left(\frac{1}{5} \phi_{s\ell}^5 - \frac{2}{3} \phi_{s\ell}^3 + \phi_{s\ell} \right), \tag{20}$$

and thus $P(1) = 0$ and $P(-1) = 1$, so that in the solid phase $e_{s\ell}(T, 1) = e_s(T)$, and in the liquid phase $e_{s\ell}(T, -1) = e_\ell(T)$. By applying the interpolation function P, the continuous Flory's parameter can be defined as a similar form across the interface:

$$\langle \chi_i \rangle = P \chi_{i,\ell} + (1 - P) \langle \chi_{i,s} \rangle, \tag{21}$$

where $\langle \chi_{i,s} \rangle > \chi_{i,\ell}$, in which a higher value of the Flory's parameter implies a higher mixing energy in the ice phase than in liquid water so that the solutes are soluble, within the solubility limit, in the liquid phase and mostly excluded from ice. Although a part of the excluded solutes are trapped in between ice crystals, the small scale phenomena is not resolved in this simplified macroscopic model and therefore a phenomenological $\langle \chi_{i,s} \rangle$ value is proposed in this study. In principle, the phenomenological value may be estimated by the mesoscale analysis by considering crystal morphology and segregation pattern under various cooling conditions, or to be adjusted based on empirical results.

From Eqs. (18) and (19), the left-hand side of the energy equation (Eq. (9)) can be further expanded from the interpolation of internal energy across each phase using the P function along with the material derivative, expressed as

$$\frac{\mathrm{D}e}{\mathrm{D}t} \simeq P\frac{\mathrm{D}e_\ell}{\mathrm{D}t} + (1-P)\frac{\mathrm{D}e_s}{\mathrm{D}t} + RT\sum_{i=1}^{n}\langle\chi_i\rangle(1-2\phi_i)\frac{\mathrm{D}\phi_i}{\mathrm{D}t} + \left[L_aP' + RT\sum_{i=1}^{n}\langle\chi_i\rangle'\phi_i(1-\phi_i)\right]\frac{\mathrm{D}\phi_{s\ell}}{\mathrm{D}t}. \tag{22}$$

By introducing heat conduction flux and specific heat, $c_p \simeq c_p(T, \phi_{s\ell}, \phi_1)$ for both solid and liquid phases, into the energy equation, the temperature equation becomes

$$\rho c_p\frac{\mathrm{D}T}{\mathrm{D}t} \simeq \nabla\cdot\left(k\nabla T\right) - \rho RT\sum_{i=1}^{n}\langle\chi_i\rangle(1-2\phi_i)\frac{\mathrm{D}\phi_i}{\mathrm{D}t} - \rho\left[L_aP' + RT\sum_{i=1}^{n}\langle\chi_i\rangle'\phi_i(1-\phi_i)\right]\frac{\mathrm{D}\phi_{s\ell}}{\mathrm{D}t}. \tag{23}$$

Assuming that the proteins at low concentration does not influence thermophysical properties of the solution, the local values of specific heat c_p and thermal conductivity k are temperature-dependent and only adjusted by the sucrose (as the primary solute, $i = 1$) content according to

$$c_p(T, \phi_{s\ell}, \phi_1) = c_{p0}\widetilde{c_p} \simeq c_{p0}\left[P\widetilde{c}_{p_\ell}(T, \phi_1) + (1-P)\widetilde{c}_{p_s}(T)\right], \tag{24}$$

and

$$k(T, \phi_{s\ell}, \phi_1) = k_0\widetilde{k} \simeq k_0\left[P\widetilde{k}_\ell(T, \phi_1) + (1-P)\widetilde{k}_s(T)\right], \tag{25}$$

where $c_{p0} = c_{p_s}(T \to T_0)$ and $k_0 = k_s(T \to T_0)$ are reference values at equilibrium freezing temperature of pure water.

2.4. Free energy and phase-field equations

The derivatives of the internal energy appeared in the phase-field Eqs. (7) and (8) can be obtained by the corresponding derivatives of the free energy density as

$$\frac{\partial e}{\partial\phi_{s\ell}})_{s,\phi_1,\phi_2,\ldots,\phi_n} = \frac{\partial f}{\partial\phi_{s\ell}})_{T,\phi_1,\phi_2,\ldots,\phi_n} \tag{26}$$

and

$$\frac{\partial e}{\partial\phi_i})_{s,\phi_{s\ell},\phi_{j,j\neq i}} = \frac{\partial f}{\partial\phi_i})_{T,\phi_{s\ell},\phi_{j,j\neq i}} \quad \text{for} \quad i, j = 1, 2, \ldots, n. \tag{27}$$

Here the continuous free energy density includes the free energy of ice and liquid phases, adjusted by solute and mixing effects. By superposing the contributions of pure solid and liquid water, sucrose and proteins, and the mixing entropy and enthalpy effects, the mean-field approximation of the free energy can be estimated by

$$f(T, \phi_{s\ell}, \phi_1, \phi_2, \ldots, \phi_n) \simeq \left(1 - \textstyle\sum_{i=1}^n \phi_i\right) f_{s\ell} + \textstyle\sum_{i=1}^n \Big\{\phi_i f_i + RT\left[\tfrac{1}{N_i}\phi_i\ln(\phi_i) + (1-\phi_i)\ln(1-\phi_i) + \langle\chi_i\rangle\phi_i(1-\phi_i)\right]\Big\}, \tag{28}$$

where $f_{s\ell}$ represents the free energy of water in ice to liquid phase, f_i is the free energy of solutes, N_i accommodates the size effect based on solute-to-water partial molar volume ratio, and the coarse-grained Flory's parameters $\langle\chi_i\rangle$ control the energy barriers in the mixing enthalpy terms for different solutes under dilute approximation. From the Gibbs-Helmholtz relation the free energy $f_{s\ell}$ including the latent heat effect can be expressed as

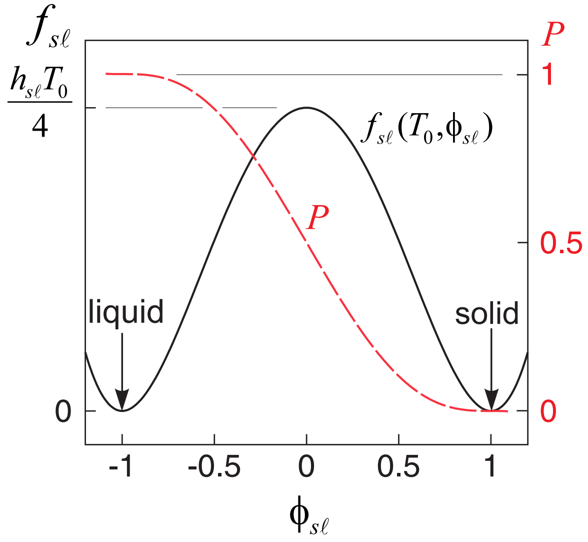

Fig. 2. Distribution of interpolation P function and the double-well potential $f_{s\ell}(T_0, \phi_{s\ell})$ at the freezing temperature of pure water. $h_{s\ell}$ is associated with the energy barrier of the solid-liquid phase transition.

$$f_{s\ell}(T, \phi_{s\ell}) = -T\int_{T_{\mathrm{eq}}}^{T}\frac{e_{s\ell}}{T'^2}dT' + \frac{Tf_{s\ell}(T_{\mathrm{eq}}, \phi_{s\ell})}{T_{\mathrm{eq}}}, \tag{29}$$

where the first term on the right-hand side presents the thermodynamic driving force on freezing. The driving force increases as the temperature is lowered, compared to the equilibrium temperature $T_{\mathrm{eq}} = T_{\mathrm{eq}}(\phi_1)$, with freezing point depression taken into account. The 2nd term accommodates the free energy at equilibrium temperature, which is approximated by a double-well potential (Fig. 2) as

$$f_{s\ell}(T_{\mathrm{eq}}, \phi_{s\ell}) = \frac{1}{4}h_{s\ell}T_{\mathrm{eq}}(1-\phi_{s\ell}^2)^2, \tag{30}$$

where the coefficient of the energy barrier $h_{s\ell}$ is associated with interfacial thickness $W_{s\ell}$ and energy coefficient $\xi_{s\ell}$ as

$$\xi_{s\ell}^2 = \rho_0 h_{s\ell}W_{s\ell}^2. \tag{31}$$

The free energy of the solution $f_{s\ell}$ has minima at $\phi_{s\ell} = -1$ (liquid) and $\phi_{s\ell} = 1$ (solid) at equilibrium freezing temperature T_{eq}.

From the internal and free energies provided above and the assumed constant latent heat L_a, the phase-field formulations, Eqs. (7) and (8), can be further expanded and written as

$$\frac{\mathrm{D}\phi_{s\ell}}{\mathrm{D}t} \simeq M_{s\ell}\Big\{\xi_{s\ell}^2\nabla^2\phi_{s\ell} - \rho R\textstyle\sum_{i=1}^n\langle\chi_i\rangle'\phi_i(1-\phi_i) + (1 - \textstyle\sum_{i=1}^n\phi_i)\left[\rho P'L_a\dfrac{T-T_{\mathrm{eq}}}{TT_{\mathrm{eq}}} + \rho h_{sl}(\phi_{s\ell} - \phi_{s\ell}^3)\right]\Big\}, \tag{32}$$

and

$$\frac{\mathrm{D}\phi_i}{\mathrm{D}t} = -\nabla\cdot\left[M_i\nabla\left(\xi_i^2\nabla^2\phi_i\right)\right] + \nabla\cdot\Big\{M_i\nabla\left[\rho R\left(\tfrac{\ln\phi_i}{N_i} - \ln(1-\phi_i) + \langle\chi_i\rangle(1-2\phi_i)\right)\right]\Big\}, \tag{33}$$

for $i = 1, 2, \ldots, n,$ respectively.

Due to the sedimentation of solutes in the liquid solution, an additional convective term is applied to the material derivative of the solute concentration equations. The rate of sedimentation is simplified by applying the Stokes' Law for a spherical particle as

$$\boldsymbol{v}_i^{\infty} = \frac{d_i^2(\rho_i - \rho_\ell)\boldsymbol{g}}{18\eta}, \tag{34}$$

where d_i is the hydrodynamic diameter of the solute molecule, $\eta = \eta(T, \phi_{s\ell}, \phi_1)$ is the local dynamic viscosity, and $\boldsymbol{g}$ is gravity acceleration. Therefore, the concentration equation becomes

$$\begin{aligned} &\frac{\partial \phi_i}{\partial t} + \boldsymbol{v} \cdot \nabla\phi_i + \nabla \cdot \left(\boldsymbol{v}_i^{\infty}\phi_i\right) = -\nabla \cdot \left[M_i \nabla\left(\xi_i^2 \nabla^2 \phi_i\right)\right] \\ &+\nabla \cdot \left\{M_i \nabla\left[\rho R\left(\frac{\ln\phi_i}{N_i} - \ln(1-\phi_i) + \langle\chi_i\rangle(1-2\phi_i)\right)\right]\right\} \end{aligned} \tag{35}$$

for $i = 1, 2, \ldots, n$.

Finally, the gradient coefficient $\xi_{s\ell}$ is associated with interfacial conditions of the freezing front. The interfacial energy $\gamma_{s\ell}$ and thickness $W_{s\ell}$ are correlated with the coefficient as

$$\gamma_{s\ell} = \frac{2\sqrt{2}}{3}\frac{\xi_{s\ell}^2 T_0}{W_{s\ell}}, \tag{36}$$

where the factor $2\sqrt{2}/3$ is derived from the one-dimensional approximation using a hyperbolic function to describe the phase field profiles $\phi_{s\ell}$ (defined from -1 to 1) across the interface at equilibrium, which is

$$\gamma_{s\ell} = T_0 \xi_{s\ell}^2 \int_{-\infty}^{\infty} \left(\frac{d\phi_{s\ell}}{dx}\right)^2 dx. \tag{37}$$

The coefficient ξ_i is assumed the same value as $\xi_{s\ell}$ for all solutes. The solute distribution described by the Cahn-Hilliard equation is conserved, and the 2nd-order derivative is consistent with the Fickian-type diffusion model by defining mobility coefficient as

$$M_i = \frac{\mathcal{D}_i(T, \phi_{s\ell}, \phi_i)}{\rho R}\phi_i(1-\phi_i) \quad \text{for} \quad i = 1, 2, \ldots, n, \tag{38}$$

where the diffusivity $\mathcal{D}_i$, assumed independent of other solutes in the dilute regime, can be in general scaled and interpolated as

$$\begin{aligned} \mathcal{D}_i(T, \phi_{s\ell}, \phi_i) &= \mathcal{D}_0 \widetilde{\mathcal{D}}_i \\ &\simeq \mathcal{D}_0\left[P\widetilde{\mathcal{D}}_{i\ell}(T, \phi_i) + (1-P)\widetilde{\mathcal{D}}_{is} + \widetilde{\mathcal{D}}_{\text{inter}}\right], \end{aligned} \tag{39}$$

where $\widetilde{\mathcal{D}}_{i\ell}$ is concentration- and temperature-dependent in liquid solution, $\widetilde{\mathcal{D}}_{is}$ is assumed constant in ice, $\widetilde{\mathcal{D}}_{\text{inter}}$ is an additional high diffusivity at the ice/freeze-concentrate interface, and all are scaled by a reference value $\mathcal{D}_0 = \mathcal{D}_{1\ell}(\phi_1 \to 0,\ T = T_0)$, where the subscript 1 indicates sucrose. Here, an adjustable diffusivity at the interface $\mathcal{D}_{\text{inter}}$ is applied to accommodate solute exclusion effect across the interface, expressed as

$$\mathcal{D}_{\text{inter}} \simeq \mathcal{D}^{\infty} F(\phi_{s\ell}) K(v_n), \tag{40}$$

where $\mathcal{D}^{\infty} \gg \mathcal{D}_0$ is to accommodate equilibrium interfacial kinetics, $F(\phi_{s\ell}) = (1 - \phi_{s\ell}^2)^{\beta_1}$ is used to locate $\mathcal{D}_{\text{inter}}$ to the interface region with a factor β_1 to adjust the area thickness, $v_n \simeq |\partial\phi_{s\ell}/\partial t|$ is the absolute value of the normal-to-interface velocity, and $K(v_n) = (1 + \beta_2 v_n)^{-1}$ determines the negative correlation of the solute exclusion effect by taking the ice front velocity into account using a weighting factor β_2. In this study, $\mathcal{D}^{\infty} \simeq 10^{-6}$ m^2/s, and the factors $\beta_1 = 8$ and $\beta_2 = 5$.

2.5. Scaled formulation

To extract further insights into the quantitative analysis, all computations are carried out based on the scaled formulation as follows. The length scale is defined by the radius of the vessel R_i.

Table 1
Parameters and properties used in the test cases. The model protein is assumed bovine serum albumin (BSA) since it is commonly used in protein solutions to stabilize therapeutic biologics.

Parameters	Value, SI
length scale R_i (inner radius of vessel)	0.025 m
interfacial thickness $W_{s\ell}$	0.001 m
characteristic subcooled temperature $\triangle T$	10 K
initial temperature T_ini	283.15 K
fixed environmental temperature T_env	253.15 K
latent heat L_a	3.4×10^5 J/kg
Flory's parameters of sucrose $\langle\chi_{1,s}\rangle$, $\chi_{1,\ell}$	0.6, 0.5
Flory's parameters of protein $\langle\chi_{2,s}\rangle$, $\chi_{2,\ell}$	0.501, 0.5
solute-to-water ratio of molar volume for sucrose N_1	~ 11.5
solute-to-water ratio of molar volume for protein N_2	~ 2300
interfacial energy $\gamma_{s\ell}$ [44]	0.041 J/m^2
energy barrier coefficient $h_{s\ell}$	0.064 J/(kg · K)
characteristic density variation $\triangle\rho$	5 kg/m^3
characteriatic velocity U	6.0×10^{-3} m/s
diameter of sucrose d_1	10^{-9} m
diameter of protein d_2	7.0×10^{-9} m
thermal conductivity of steel k_steel	15.06 W/(m · K)
thermal conductivity of air k_air	0.0223 W/(m · K)

The apparent interfacial thickness $W_{s\ell}$ is assumed much smaller than R_i. The system involves six characteristic time scales for solid-liquid phase transition, solute diffusion, thermal diffusion, sedimentation, viscous diffusion, and bulk convection, respectively, defined as

$$\begin{aligned} &\tau_{s\ell} = \frac{1}{\rho_0 h_{s\ell} M_{s\ell}}, \quad \tau_c = \frac{R_\text{i}^2}{\mathcal{D}_0}, \quad \tau_{\text{T}} = \frac{\rho_0 c_{p0} R_\text{i}^2}{k_0} = \frac{R_\text{i}^2}{\alpha_0}, \\ &\tau_\text{sed} = \frac{18\eta_0 R_\text{i}}{\rho_0 d_1^2 g}, \quad \tau_\text{vis} = \frac{\rho_0 R_\text{i}^2}{\eta_0}, \quad \text{and} \quad \tau_\text{conv} = \frac{R_\text{i}}{U}, \end{aligned} \tag{41}$$

respectively, where d_1 is a reference diameter of solutes based on sucrose molecule, $\alpha_0 = k_0/(\rho_0 c_{p0})$ is the reference thermal diffusivity at T_0, and U is the characteristic velocity estimated from the Stokes flow as

$$U = \frac{2W_{s\ell}^2 g \triangle\rho}{9\eta_0}, \tag{42}$$

where $\triangle\rho$ is the characteristic density variation, assumed 5 kg/m^3 based on one percent increase of sucrose concentration in this study. The temperature is scaled by the characteristic subcooled temperature $\triangle T$ as

$$\widetilde{T} = \frac{T - T_0}{\triangle T}. \tag{43}$$

The pressure and stress are scaled by viscous effect based on the reference viscosity. The vorticity and stream function are scaled by U/R_i and UR_i^2, respectively. The phase field $\phi_{s\ell}$ and species concentration ϕ_i are already normalized. The actual value of mobility $M_{s\ell}$ in the $\phi_{s\ell}$ equation for the macroscopic analysis is unknown, here we speculate that the freezing process is largely controlled by thermal transport and thus the time scale for solid-liquid phase transition is assumed the same as the thermal diffusion time, $\tau_{s\ell} \simeq \tau_{\text{T}}$. The characteristic time scale τ_{T} is selected for all of the scaled formulations. The parameters, time scales, and reference properties are listed in Tables 1–3 for reference.

The resulting scaled vorticity and stream-function equations are

$$\begin{aligned} &\widetilde{\rho}\left(\frac{1}{\mathcal{P}_\text{r}}\frac{\partial\widetilde{\boldsymbol{\omega}}}{\partial\widetilde{t}} + \mathcal{R}_\text{e}\widetilde{\boldsymbol{v}} \cdot \widetilde{\nabla}\widetilde{\boldsymbol{\omega}}\right) = \widetilde{\eta}\widetilde{\nabla}^2\widetilde{\boldsymbol{\omega}} + \widetilde{\nabla}\widetilde{\eta} \times \widetilde{\nabla}^2\widetilde{\boldsymbol{v}} \\ &+\widetilde{\nabla} \times \left[\widetilde{\nabla}\widetilde{\eta} \cdot \left(\widetilde{\nabla}\widetilde{\boldsymbol{v}} + \widetilde{\nabla}\widetilde{\boldsymbol{v}}^{\text{T}}\right)\right] + \widetilde{\nabla} \times (\mathcal{G}_\text{r}\hat{\mathbf{e}}_z), \end{aligned} \tag{44}$$

Table 2
Reference properties of pure water at ambient pressure.

Reference properties	Value, SI
freezing temperature T_0	273.15 K
density ρ_0	999.8 kg/m^3
specific heat c_{p0}	2110 J/(kg · K)
thermal conductivity k_0	2.15 W/(m · K)
dynamic viscosity η_0	1.8×10^{-3} Pa · s
solute diffusivity $\mathcal{D}_0$	2.1×10^{-10} m^2/s

Table 3
Characteristic time scales based on parameters listed in Table 1.

Characteristic times	Value, SI
thermal diffusion τ_{T}	616.11 s
phase transition $\tau_{s\ell}$	616.11 s
solute diffusion τ_c	2.98×10^6 s
bulk convection τ_{conv}	4.17 s
viscous diffusion τ_{vis}	347.15 s
sedimentation τ_{sed}	8.26×10^{10} s

and

$$\frac{\partial^2 \tilde{\psi}}{\partial \tilde{z}^2} + \frac{\partial^2 \tilde{\psi}}{\partial \tilde{r}^2} - \frac{1}{\tilde{r}} \frac{\partial \tilde{\psi}}{\partial \tilde{r}} = -\tilde{\omega}\tilde{r}, \tag{45}$$

respectively, where $\hat{\mathbf{e}}_z$ indicates unit vector in z direction. The Prandtl number $\mathcal{P}_{\mathrm{r}}$ is the ratio of the thermal to viscous time scales, Reynolds number $\mathcal{R}_{\mathrm{e}}$ compares the inertial to viscous effects, and the local Grashof number $\mathcal{G}_{\mathrm{r}}$ depends on the local density $\tilde{\rho}$ and the buoyant to viscous effect. They can be defined as

$$\mathcal{P}_{\mathrm{r}} = \frac{\eta_0}{\rho_0 \alpha_0} = \frac{\tau_{\mathrm{T}}}{\tau_{\mathrm{vis}}}, \quad \mathcal{R}_{\mathrm{e}} = \frac{\rho_0 U R_{\mathrm{i}}}{\eta_0} = \frac{\tau_{\mathrm{vis}}}{\tau_{\mathrm{conv}}}, \quad \text{and} \quad \mathcal{G}_{\mathrm{r}} = \frac{\rho_0 R_{\mathrm{i}}^2 g (1-\tilde{\rho})}{\eta_0 U}, \tag{46}$$

respectively.

The scaled phase-field equations reduce to

$$\begin{aligned} \frac{\partial \phi_{s\ell}}{\partial \tilde{t}} + \mathcal{P}_{\mathrm{e}} \tilde{\boldsymbol{v}} \cdot \tilde{\nabla} \phi_{s\ell} &= \mathcal{C}_{\mathrm{h}}^2 \tilde{\nabla}^2 \phi_{s\ell} \\ &+ \Lambda_{s\ell} \left(1 - \sum_{i=1}^{n} \phi_i \right) P' \left\{ \frac{\tilde{T} - \tilde{T}_{\mathrm{eq}}}{\left[1 + (\triangle T/T_0)\ \tilde{T}\right]\left[1 + (\triangle T/T_0)\ \tilde{T}_{\mathrm{eq}}\right]} \right\} \\ &+ (1 - \sum_{i=1}^{n} \phi_i)(\phi_{s\ell} - \phi_{s\ell}^3) - \frac{R}{h_{s\ell}} \sum_{i=1}^{n} \langle \chi_i \rangle' \phi_i (1 - \phi_i), \end{aligned} \tag{47}$$

and

$$\begin{aligned} \frac{\partial \phi_i}{\partial \tilde{t}} &+ \mathcal{P}_{\mathrm{e}} \tilde{\boldsymbol{v}} \cdot \tilde{\nabla} \phi_i + \Lambda_{\mathrm{sed}} \tilde{\nabla} \cdot \left[\frac{\tilde{d}_i^2}{\tilde{\eta}} (\tilde{\rho}_\ell - \tilde{\rho}_i) \phi_i \hat{\mathbf{e}}_z \right] \\ &= -\frac{\mathcal{C}_{\mathrm{h}}^2}{\mathcal{L}_{\mathrm{e}}} \frac{h_{s\ell}}{R} \tilde{\nabla} \cdot \left\{ \tilde{\mathcal{D}}_i (\phi_i - \phi_i^2) \tilde{\nabla} \tilde{\nabla}^2 \phi_i \right\} \\ &\quad + \frac{1}{\mathcal{L}_{\mathrm{e}}} \tilde{\nabla} \cdot \left\{ \tilde{\mathcal{D}}_i \left[\frac{1 - \phi_i}{N_i} + \phi_i - 2(\phi_i - \phi_i^2) \langle \chi_i \rangle \right] \tilde{\nabla} \phi_i \right\} \\ &\quad + \frac{1}{\mathcal{L}_{\mathrm{e}}} \tilde{\nabla} \cdot \left[\tilde{\mathcal{D}}_i (\phi_i - \phi_i^2)(1 - 2\phi_i) \tilde{\nabla} \langle \chi_i \rangle \right] \end{aligned} \tag{48}$$

for $i = 1, 2, \ldots, n$, where the Peclet number $\mathcal{P}_{\mathrm{e}}$ measures convective to diffusive effects and applicable to mass transport of all solutes, phase-change number $\Lambda_{s\ell}$ measures the importance of latent heat to interfacial energy, Cahn-Hilliard number $\mathcal{C}_{\mathrm{h}}$ is the ratio of the interfacial thickness to the length scale, sedimentation number Λ_{sed} compares the time scales of thermal diffusion to sedimentation, whereas Lewis number $\mathcal{L}_{\mathrm{e}}$ compares thermal diffusivity to mass diffusivity. These dimensionless groups are defined as

$$\mathcal{P}_{\mathrm{e}} = \frac{R_{\mathrm{i}} U}{\alpha_0} = \frac{\tau_{\mathrm{T}}}{\tau_{\mathrm{conv}}}, \quad \Lambda_{s\ell} = \frac{L_a \triangle T}{h_{s\ell} T_0^2}, \quad \mathcal{C}_{\mathrm{h}} = \frac{W_{s\ell}}{R_{\mathrm{i}}}, \quad \Lambda_{\mathrm{sed}} = \frac{\rho_0 d_0^2\, g R_{\mathrm{i}}}{18 \eta_0 \alpha_0} = \frac{\tau_{\mathrm{T}}}{\tau_{\mathrm{sed}}}, \quad \text{and} \quad \mathcal{L}_{\mathrm{e}} = \frac{\alpha_0}{\mathcal{D}_0} = \frac{\tau_c}{\tau_{\mathrm{T}}}, \tag{49}$$

respectively.

Furthermore, the scaled thermal energy equation becomes

$$\begin{aligned} &\tilde{\rho} \tilde{c}_p \left(\frac{\partial \tilde{T}}{\partial \tilde{t}} + \mathcal{P}_{\mathrm{e}} \tilde{\boldsymbol{v}} \cdot \tilde{\nabla} \tilde{T} \right) = \tilde{\nabla} \cdot \left(\tilde{k} \tilde{\nabla} \tilde{T} \right) \\ &- \frac{\tilde{\rho}}{\mathcal{S}_{\mathrm{te1}}} \left[P'(\phi_{s\ell}) + \mathcal{S}_{\mathrm{te2}} \left(\tilde{T} + \frac{T_0}{\triangle T} \right) \sum_{i=1}^{n} \langle \chi_i \rangle' \phi_i (1 - \phi_i) \right] \\ &\times \left(\frac{\partial \phi_{s\ell}}{\partial \tilde{t}} + \mathcal{P}_{\mathrm{e}} \tilde{\boldsymbol{v}} \cdot \tilde{\nabla} \phi_{s\ell} \right) \\ &- \frac{\tilde{\rho} \mathcal{S}_{\mathrm{te2}}}{\mathcal{S}_{\mathrm{te1}}} \left(\tilde{T} + \frac{T_0}{\triangle T} \right) \sum_{i=1}^{n} \langle \chi_i \rangle (1 - 2\phi_i) \left(\frac{\partial \phi_i}{\partial \tilde{t}} + \mathcal{P}_{\mathrm{e}} \tilde{\boldsymbol{v}} \cdot \tilde{\nabla} \phi_i \right), \end{aligned} \tag{50}$$

where the Stefan numbers $\mathcal{S}_{\mathrm{te1}}$ and $\mathcal{S}_{\mathrm{te2}}$ compare the latent heat to the sensible heat and the partition effect, formulated as

$$\mathcal{S}_{\mathrm{te1}} = \frac{c_{p0} \triangle T}{L_a} \quad \text{and} \quad \mathcal{S}_{\mathrm{te2}} = \frac{R \triangle T}{L_a}, \tag{51}$$

respectively. Values of these dimensionless groups are listed in Table 4.

2.6. Initial and boundary conditions

The configuration and basic dimensions of the cylindrical vessel shown in Fig. 3 is extracted from experimental setting provided by Rodrigues el al. [15], so that we can side-by-side compare the computational results with experimental data. The computational domain Ω is shown by the blue area with initial conditions defined by uniform temperature T_{ini} and uniform concentration $\phi_{i,\mathrm{ini}}$ in a quiescent liquid solution. There exists no ice phase at T_{ini}. The environmental temperature T_{env} is assumed constant during the cooling and freezing processes.

Boundary conditions for the conserved phase fields ϕ_i are insulated (zero mass flux) for all of the four boundaries, including the top, bottom, and circumferential side wall as well as the symmetric axis. The stream function vanishes at all boundaries, meanwhile the velocity satisfies no-slip conditions on top, bottom, and circumferential wall boundaries. The vorticity on the boundaries follows $\boldsymbol{\omega} = \nabla \times \mathrm{v}$. In phase-field method, the velocity in the solid region, $\phi_{s\ell} = 1$, vanishes across the ice/freeze-concentrate interface. In this study, we apply a smooth function for the vorticity and stream function to approximate the stationary solid phase, ex-

Table 4
Dimensionless groups with values based on parameters listed in Table 1.

Dimensionless groups	Value
Prandtl number $\mathcal{P}_{\mathrm{r}}$	1.775
Reynolds number $\mathcal{R}_{\mathrm{e}}$	83.32
local Grashof number $\mathcal{G}_{\mathrm{r}}$	$5.67 \times 10^5 (1 - \tilde{\rho})$
Peclet number $\mathcal{P}_{\mathrm{e}}$	147.87
phase-change number $\Lambda_{s\ell}$	715.33
Cahn-Hilliard number $\mathcal{C}_{\mathrm{h}}$	0.04
Lewis number $\mathcal{L}_{\mathrm{e}}$	4830.6
sedimentation number Λ_{sed}	7×10^{-9}
Stefan number $\mathcal{S}_{\mathrm{te1}}$	0.0621
Stefan number $\mathcal{S}_{\mathrm{te2}}$	0.0136

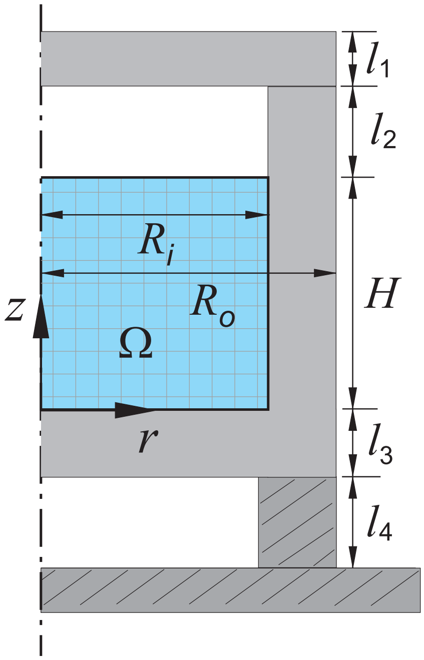

Fig. 3. Geometry of the cylindrical vessel: inner radius $R_i = 0.025$ m, outer radius $R_o = 0.0325$ m, height of solution $H = 0.0255$ m, thickness of cover lid $l_1 = 0.006$ m, vessel wall $l_3 = 0.0075$ m, and stagnant air layer $l_2 \simeq l_4 = 0.01$ m. The computational domain Ω indicates $0 \le r \le R_i$ and $0 \le z \le H$, where inner radius R_i is used as the length scale in dimensionless formulation.

pressed as

$$\tilde\omega = \tilde\omega_\ell \left[\frac{1}{2} - \frac{1}{2}\tanh\frac{\sqrt{2}(\phi_{s\ell}+0.8)}{2\mathcal{C}_h}\right] \tag{52}$$

and

$$\tilde\psi = \tilde\psi_\ell \left[\frac{1}{2} - \frac{1}{2}\tanh\frac{\sqrt{2}(\phi_{s\ell}+0.8)}{2\mathcal{C}_h}\right], \tag{53}$$

respectively. The vorticity and stream function thus have a smooth transition from liquid phase to zero in the solid phase ($\tilde\omega, \tilde\psi \to 0$ as $\phi_{s\ell} \to 1$ and $\tilde\omega \to \tilde\omega_\ell$, $\tilde\psi \to \tilde\psi_\ell$ as $\phi_{s\ell} \to -1$).

The phase fields $\phi_{s\ell}$ and ϕ_i and temperature T have zero gradient value along the radial direction at $r = 0$ as a symmetric condition. The phase field $\phi_{s\ell}$ remains -1 (liquid) on top, bottom, and circumferential wall, and only turns into 1 while the temperature on the boundaries is lower than freezing temperature T_0, indicating an immediate heterogeneous nucleation of the ice phase without supercool.

To facilitate the computation by including more general effect from heat transfer surfaces, we consider a reduced-order (nonlocal) heat transfer resistance model [45] to the top, bottom, and circumferential walls:

(i) At the top surface, $z = H$, a stagnate air layer with thickness l_2 and thermal conductivity $k_{\rm air}$ is applied. The cover lid has thickness l_1, thermal conductivity $k_{\rm steel}$, and heat exchange from natural convection to environment at temperature $T_{\rm env}$. The boundary condition is therefore formulated as

$$-k\frac{\partial T}{\partial z} = \frac{T - T_{\rm env}}{l_1/k_{\rm steel} + l_2/k_{\rm air} + 1/h_{\rm top}}, \tag{54}$$

where $h_{\rm top}$ (Fig. 1) is the heat transfer coefficient approximated by a horizontal round plate using the empirical relationship [46]:

$$\mathcal{N}_{\rm u,top} = \frac{h_{\rm top}R_i}{k_{\rm air}} \simeq 0.559\mathcal{R}_a^{1/5}, \tag{55}$$

where $\mathcal{N}_{\rm u,top}$ and $\mathcal{R}_a$ are Nusselt and Rayleigh numbers. The corresponding dimensionless form is written as

$$\frac{\partial\tilde T}{\partial\tilde z} = \frac{\tilde T_{\rm env} - \tilde T}{\tilde k\left[\tilde l_1/\tilde k_{\rm steel} + \tilde l_2/\tilde k_{\rm air} + 1/\mathcal{B}_{\rm i,top}\right]} \quad \text{at} \quad \tilde z = \tilde H, \tag{56}$$

where the Biot number $\mathcal{B}_{\rm i,top}$ is defined as

$$\mathcal{B}_{\rm i,top} = \frac{h_{\rm top}R_i}{k_0}, \tag{57}$$

indicating the conduction-to-convection resistance on the top surface.

(ii) For the bottom surface at $z = 0$, the conduction thermal resistance is based on stainless steel material with thickness l_3 and thermal conductivity $k_{\rm steel}$, and a stagnate air layer below the vessel with thickness l_4 and thermal conductivity $k_{\rm air}$. Thus the resistance boundary condition can be formulated as

$$k\frac{\partial T}{\partial z} = \frac{T - T_{\rm env}}{l_3/k_{\rm steel} + l_4/k_{\rm air}}, \tag{58}$$

and in dimensionless form:

$$\frac{\partial\tilde T}{\partial\tilde z} = \frac{\tilde T - \tilde T_{\rm env}}{\tilde k\left[\tilde l_3/\tilde k_{\rm steel} + \tilde l_4/\tilde k_{\rm air}\right]} \quad \text{at} \quad \tilde z = 0. \tag{59}$$

(iii) For the circumferential wall at $r = R_i$, conduction heat transfer through vessel and a natural convection for the vertical wall are considered, estimated by

$$-k\frac{\partial T}{\partial r} = \frac{T - T_{\rm env}}{R_i\ln(R_o/R_i)/k_{\rm steel} + R_i/(R_o h_{\rm side})}, \tag{60}$$

where R_i and R_o are the inner and outer radii of the vessel, respectively, and $h_{\rm side}$ is the heat transfer coefficient estimated by a vertical plate for a cylinder wall with large radius. An empirical relationship for a relatively small Rayleigh number ($\mathcal{R}_a \le 10^9$) can be applied to this study [45]:

$$\mathcal{N}_{\rm u,side} = \frac{h_{\rm side}H}{k_{\rm air}} \simeq 0.68 + \frac{0.67\mathcal{R}_a^{1/4}}{[1 + (0.492/\mathcal{P}_r)^{9/16}]^{4/9}}. \tag{61}$$

And the corresponding dimensionless form becomes

$$\frac{\partial\tilde T}{\partial\tilde r} = \frac{\tilde T_{\rm env} - \tilde T}{\tilde k\left[\ln(\tilde R_o)/\tilde k_{\rm steel} + 1/\left(\tilde R_o\ \mathcal{B}_{\rm i,side}\right)\right]} \quad \text{at} \quad \tilde r = 1, \tag{62}$$

where the Biot number is defined as $\mathcal{B}_{\rm i,side} = h_{\rm side}H/k_0$.

For the configuration shown in Fig. 3, the heat transfer coefficients $h_{\rm top} \simeq 4.6\,\mathrm{W/(m^2 \cdot K)}$ and $h_{\rm side} \simeq 7.9\,\mathrm{W/(m^2 \cdot K)}$, and the corresponding Biot numbers are $\mathcal{B}_{\rm i,top} \simeq 57.03$ and $\mathcal{B}_{\rm i,side} \simeq 8.37$, respectively. A reference case with fast cooling in a ethanol bath is simulated by $h_{\rm top}$, $h_{\rm side} \to \infty$.

3. Material properties

Measurements of relevant thermophysical properties of protein solutions, including density, specific heat, thermal conductivity, dynamic viscosity, and solute diffusivity within the temperature range of interest are fairly limited. Here we consider sucrose as the primary solute based on available experimental data. Although sucrose has very different properties than proteins, it is a common excipient used as a cryoprotectant in protein formulations. In this study the thermophysical properties are assumed temperature and sucrose concentration dependent, with correlations extracted from experimental data. Figs. 4 to 6 illustrate the changes of relevant material properties with temperature and sucrose concentration.

The changes of mass density in supercooled liquid water (Fig. 4a) and ice (Fig. 4b) phases are plotted against temperature.

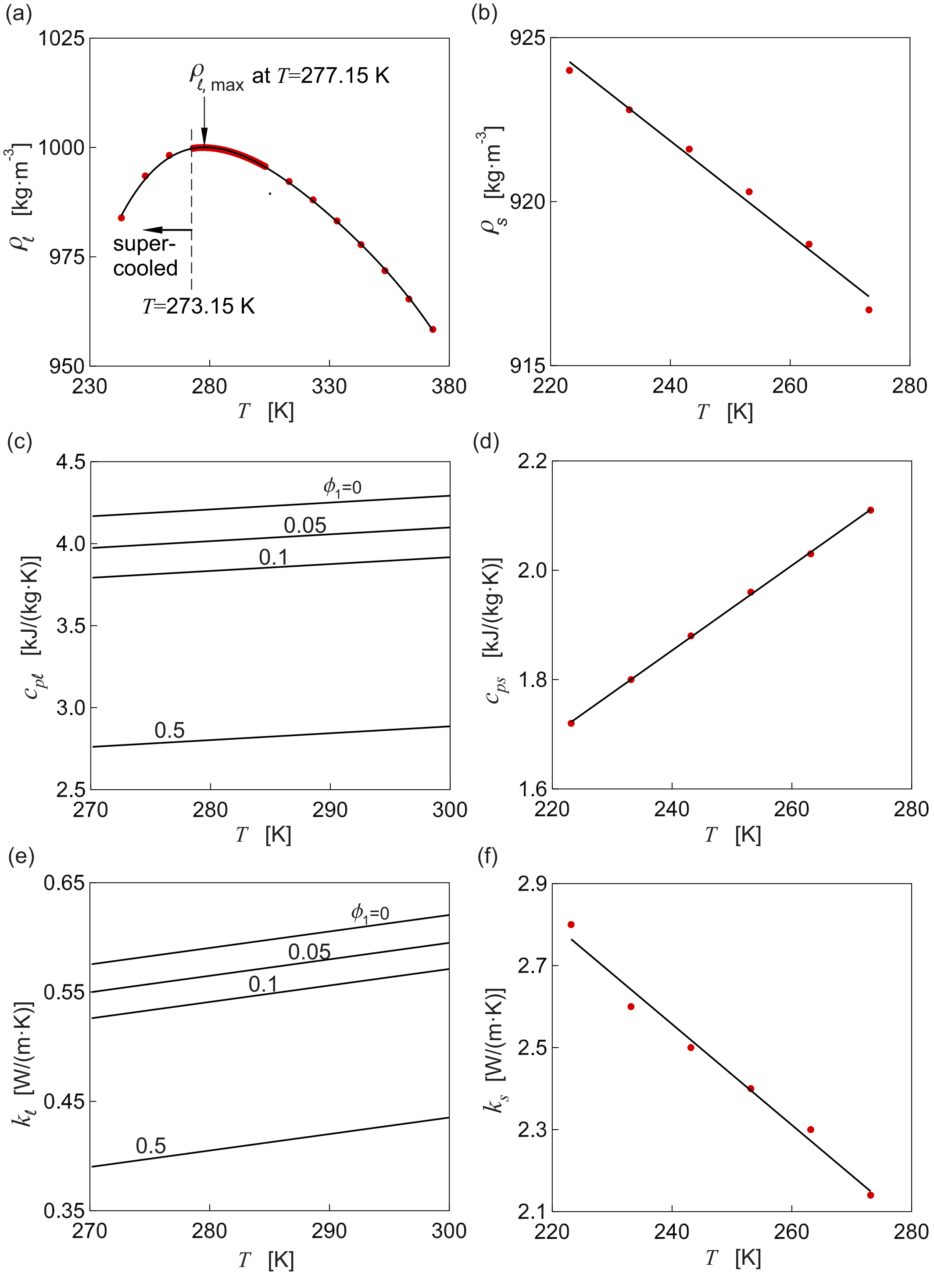

Fig. 4. Thermophysical properties. (a, b) Mass densities of pure water ρ_ℓ and ice ρ_s at different temperatures, (c, d) specific heats of sucrose solution $c_{p\ell}$ and ice c_{ps}, and (e, f) thermal conductivities of sucrose solution k_ℓ and ice k_s at different temperatures. Both $c_{p\ell}$ and k_ℓ have taken solute concentration ϕ_1 into account. All data points are from literature [47], whereas solid lines are from the correlation Eqs. (63)–(68).

The temperature dependency [47] is correlated in MKS unit as

$$\rho_\ell(T) \simeq -4\times10^{-7}(T-T_0)^4 + 10^{-4}(T-T_0)^3 \\ -0.0105(T-T_0)^2 + 0.1(T-T_0) + \rho_0, \qquad (63)$$

and

$$\rho_s(T) \simeq 0.917\rho_0 + 0.15(T_0 - T), \qquad (64)$$

respectively, where temperature is in degree Kelvin. The density in supercooled liquid state decreases a few percentages as temperature decreases. The sucrose density ρ_1 is assumed a constant 1587 kg/m^3, and the protein density ρ_2 is assumed 1364 kg/m^3 (based on BSA).

The specific heat of sucrose solution is correlated with temperature and sucrose concentration [18] as

$$c_{p_\ell}(T,\phi_1) \simeq 4180\Big[1 - 0.953\phi_1(1 - 0.588\phi_1) + 10^{-3}(T - T_0)\Big], \qquad (65)$$

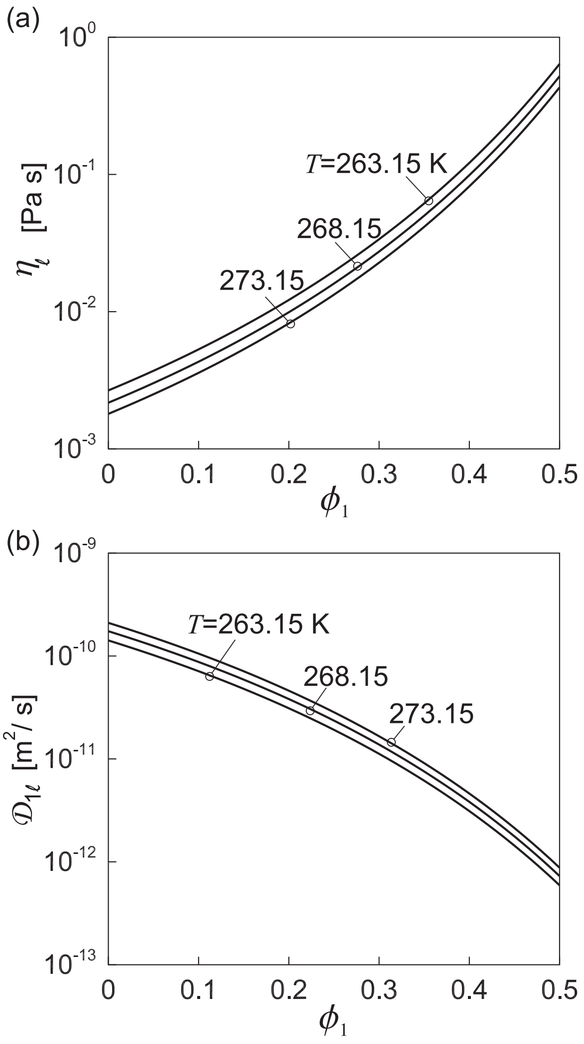

Fig. 5. Transport properties. (a) Dynamic viscosity η_ℓ and (b) diffusivity $\mathcal{D}_{1\ell}$ of sucrose in liquid solution versus its volume fraction, obtained from Eqs. (70) and (71), respectively.

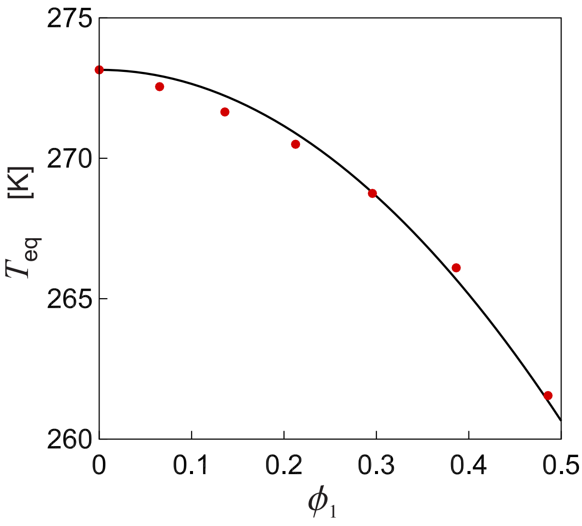

Fig. 6. Equilibrium freezing temperature T_{eq} of sucrose solution. Data points are from literature [51], whereas the solid line is based on the correlation Eq. (72).

illustrated in Fig. 4c, which monotonically increases as temperature increases. The specific heat of ice (Fig. 4d) can be correlated with temperature [47] as

$$c_{p_s}(T) \simeq c_{p0} + 7.8(T - T_0). \tag{66}$$

The thermal conductivity of sucrose solution (shown in Fig. 4e) is provided by literature [18] and expressed as

$$k_\ell(T, \phi_1) \simeq 0.58\Big[1 - 0.905\phi_1(1 - 0.588\phi_1) + 2.6 \times 10^{-3}(T - T_0)\Big], \tag{67}$$

whereas the thermal conductivity of ice (Fig. 4f) [47] can be estimated by

$$k_s(T) \simeq k_0 - 0.0123(T - T_0), \tag{68}$$

which increases as temperature decreases.

Furthermore, the temperature-dependent dynamic viscosity of water can be correlated by the Vogel-Fulcher-Tamman (VTF) model [48] as

$$\eta_\ell(T) \simeq 4.442 \times 10^{-5} \exp\left(\frac{2.288 \times 168.9}{T - 168.9}\right), \tag{69}$$

where the factor 4.442×10^{-5} is the viscosity at temperature 168.9 K ($> \ T_g \simeq 136$ K). As shown in Fig. 5a, the dynamic viscosity are negatively correlated with temperature. To incorporate the solute concentration effect to the viscosity, we compose the VTF and Mooney's viscosity models to estimate the viscosity of the sucrose solution [19] as

$$\eta_\ell(T, \phi_1) = \eta_\ell(T_0, \phi_1)\eta_\ell(T) \simeq \exp\left(\frac{6.3\phi_1}{1 - 0.85\phi_1}\right)\eta_\ell(T), \tag{70}$$

where the concentration-dependent viscosity is estimated at $T_0 =$ 273.15 K [49].

The diffusivity of sucrose in solution (Fig. 5b) can be estimated by the proportionality based on the Stokes-Einstein relation as

$$\mathcal{D}_{1\ell}(\phi_1, T) \simeq \frac{\mathcal{D}_0\ T\ \eta_0}{T_0\ \eta_\ell(\phi_1, T)}, \tag{71}$$

where $\mathcal{D}_0 \simeq 2.1 \times 10^{-10}$ m^2/s [14] is the solute diffusivity of sucrose in aqueous solution at T_0 in the dilute limit. The diffusivity for the dilute BSA protein molecules is around $\mathcal{D}_{2\ell} \simeq 5.9 \times 10^{-11}$ m^2/s [50].

Finally, the equilibrium freezing temperature of sucrose solution decreases as concentration of sucrose increases, also known as freezing-point depression, which can be estimated from the liquidus line of sucrose-water phase diagram [51] as

$$T_{\text{eq}}(\phi_1) \simeq T_0 - 50\phi_1^2, \tag{72}$$

shown in Fig. 6. The influences of dilute proteins to all properties are neglected in this study due to the lack of relevant measurement in the supercooled regime.

4. Results and discussion

The process simulation is carried out by the alternating-direction implicit (ADI) finite difference scheme for the governing Eqs. (44), (45), (47), (48), and (50) using 100 × 102 uniform mesh on a cross section of axisymmetric vessel and scaled time step 2×10^{-6}. No additional interface tracking algorithm is applied to the phase-field model. The theoretical results and discussion are arranged as follows. First, the developed phase-field methodology is validated by comparing the numerical results (shown in Fig. 7) of an axisymmtric heat conduction problem with the classical interface immobilization method, which is known robust in

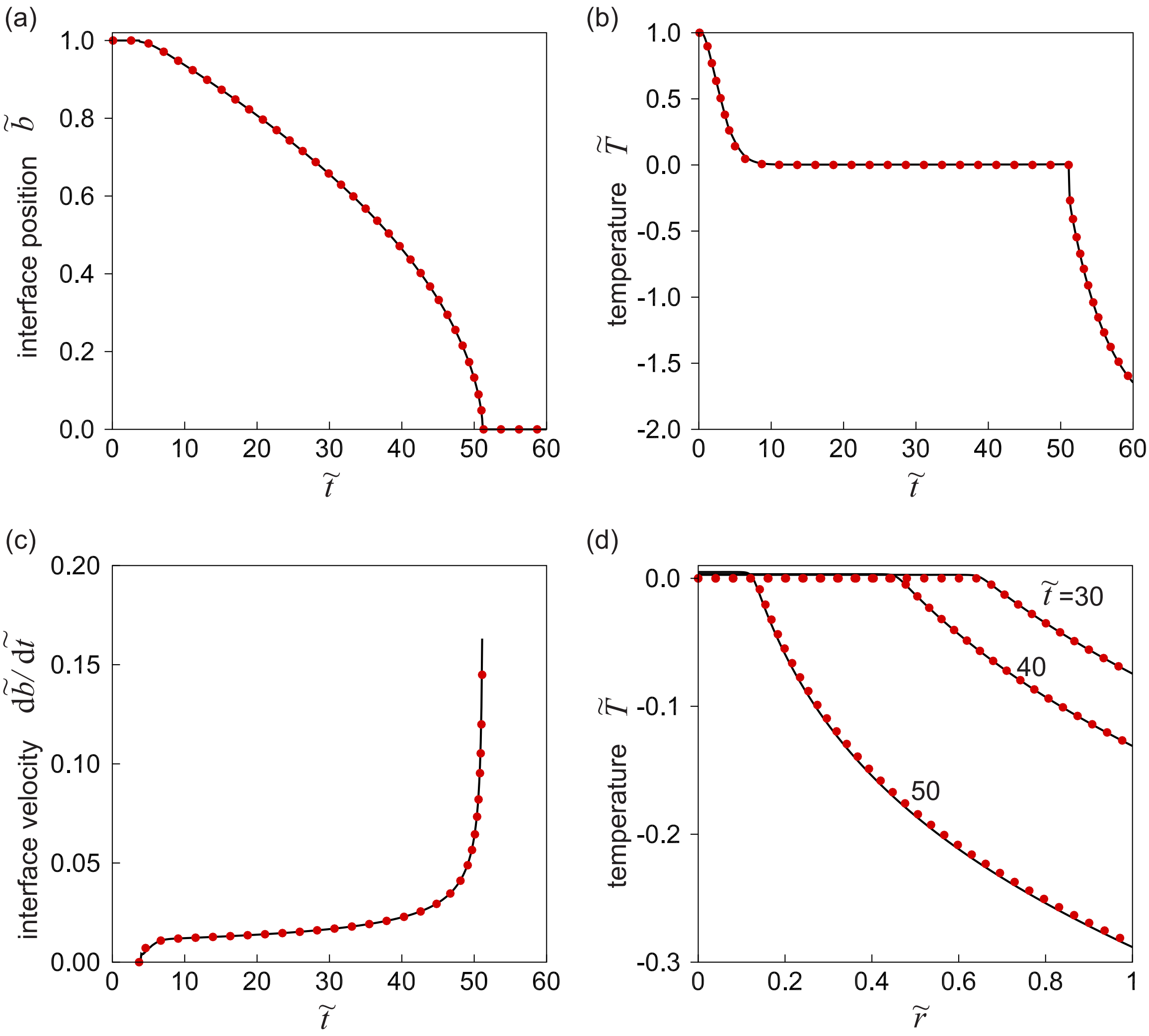

Fig. 7. Comparisons of numerical results predicted by the phase-field method (solid lines) and interface immobilization method (dots) on transient freezing dynamics of a pure water in a 1D axisymmetric domain, showing the location of the ice front along the radial direction (a), temperature at the axisymmetric center point (b), the ice front velocity (c) versus time, and the corresponding temperature profiles along the radial direction at scaled time instants $\tilde{t} = 30$, 40, and 50 (d).

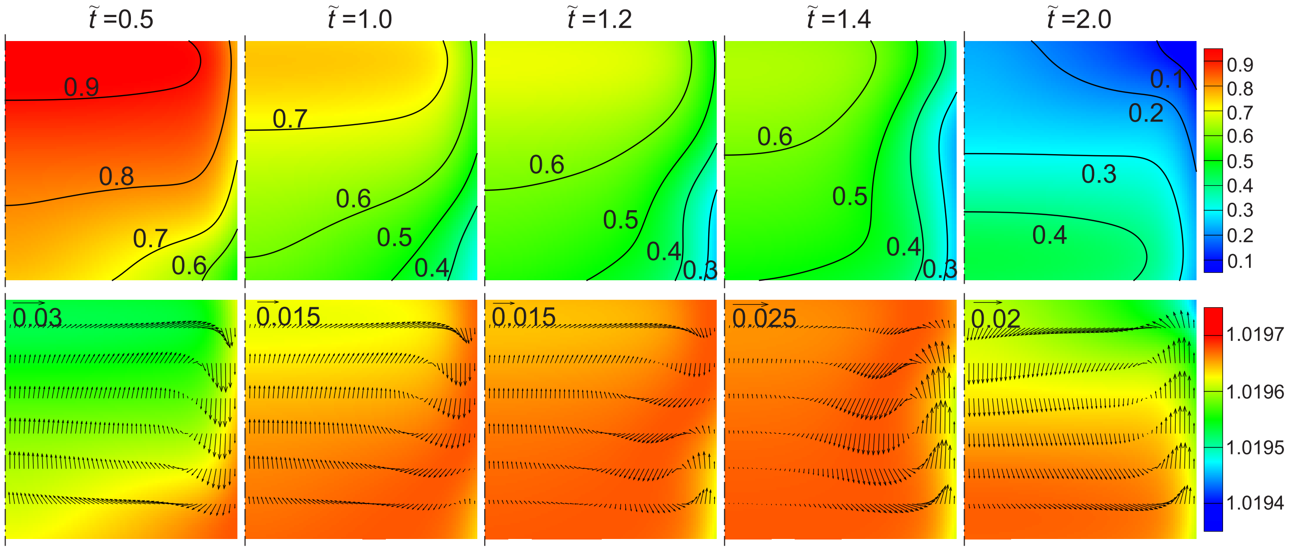

Fig. 8. Temperature field (top row, color contours) and mass density field overlapped with velocity vectors (bottom row, color contours for density) at scaled time instants $\tilde{t} = 0.5$, 1.0, 1.2, 1.4, and 2.0 during the cooling process. The ambient temperature is at $\tilde{T}_{\mathrm{env}} = -2$. The computational domain is a symmetric plane of the cylindrical vessel shown in Fig. 1.

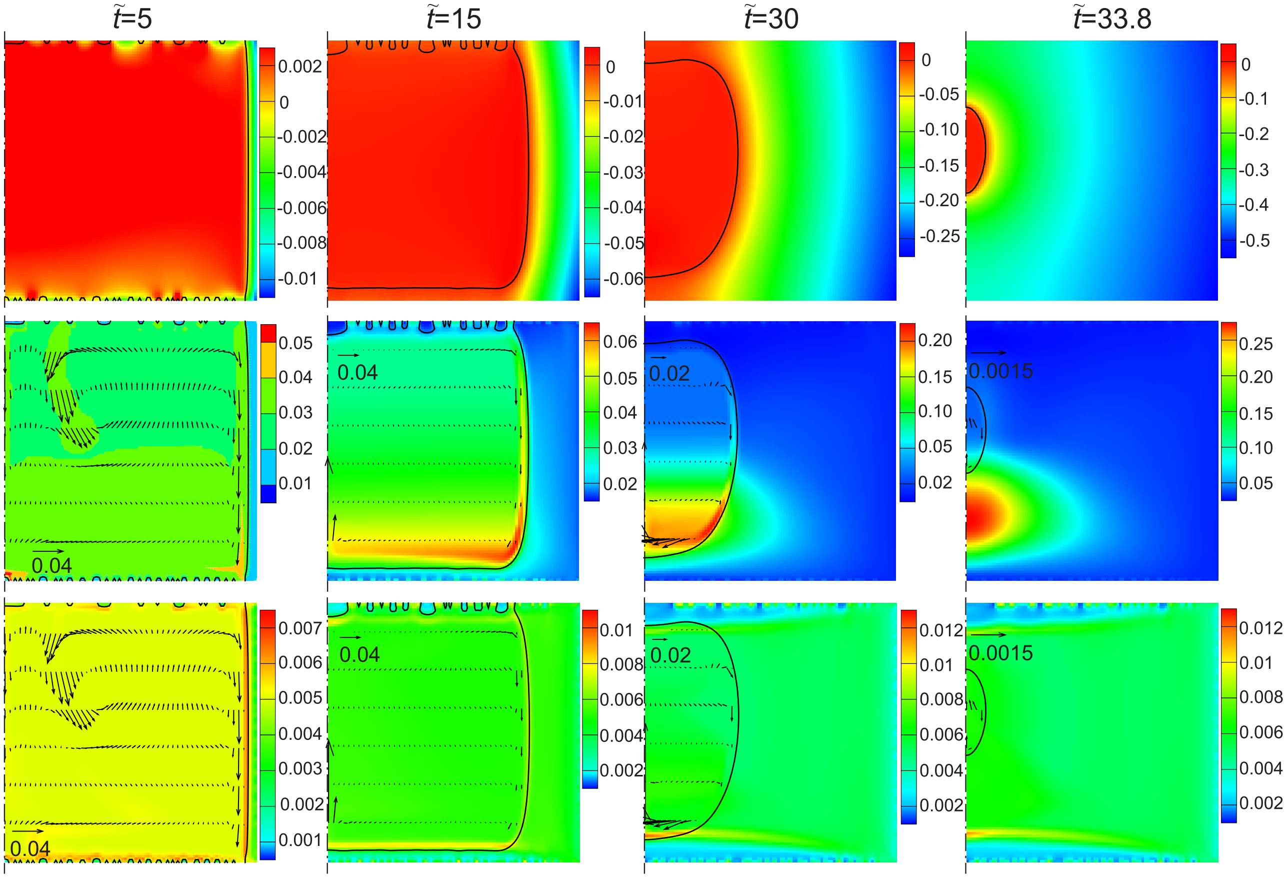

Fig. 9. Freezing dynamics in a cylindrical vessel at time instants $\tilde{t} = 5$, 15, 30, and 33.8. The top row of contour maps shows scaled temperature distribution, middle row presents sucrose volume fraction ϕ_1, and the bottom row is protein fraction ϕ_2. The contour maps on ϕ_1 and ϕ_2 are overlapped with velocity vectors of the fluid flow, and the solid lines in all results are from the phase-field prediction, indicating the ice/freeze-concentrate interfaces.

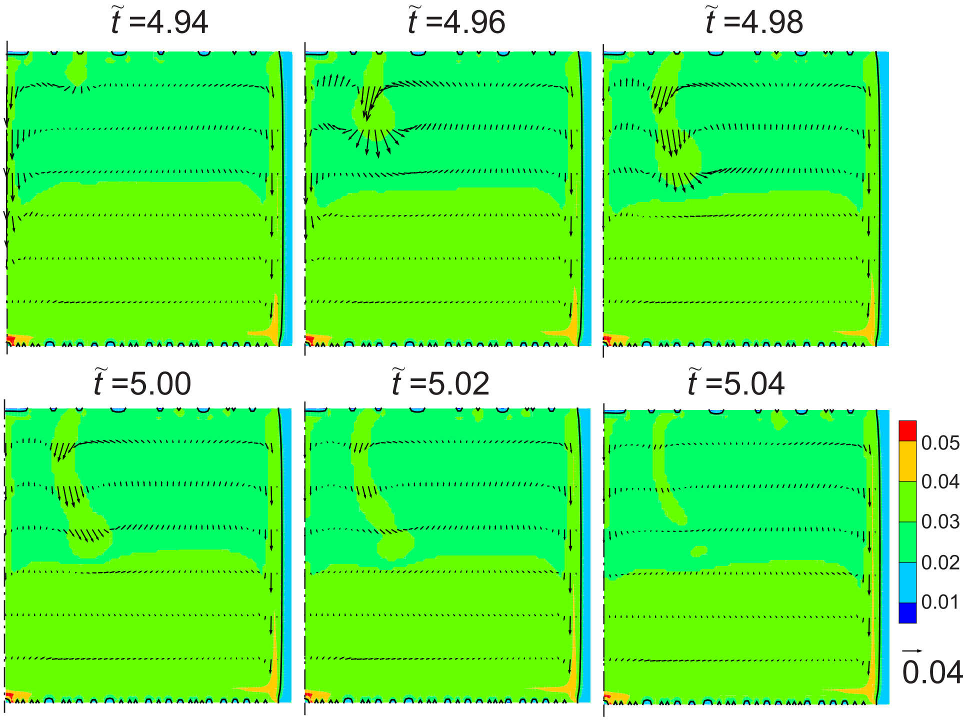

Fig. 10. An unstable flow pattern along with sucrose concentration within the vessel from $\tilde{t} = 4.94$ to 5.04. The solid lines indicate the ice/freeze-concentrate interfaces (or ice fronts).

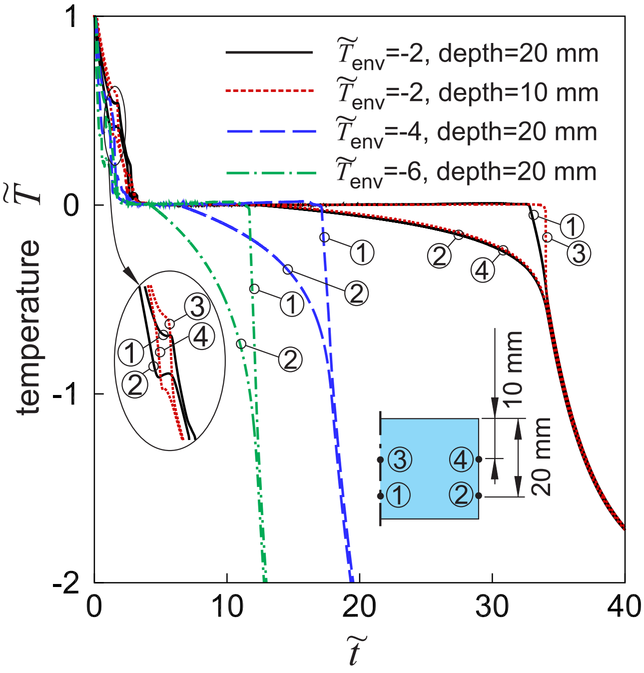

Fig. 11. Temperature histories at the specific locations along the symmetric axis and the circumferential side wall during the cooling and freezing processes under different scaled environment temperatures: $\widetilde{T}_{\rm env} = -2$, -4, and -6 (scaled by $\Delta T = 10$ K), and with time scale $\tau_T = 616.12$ s.

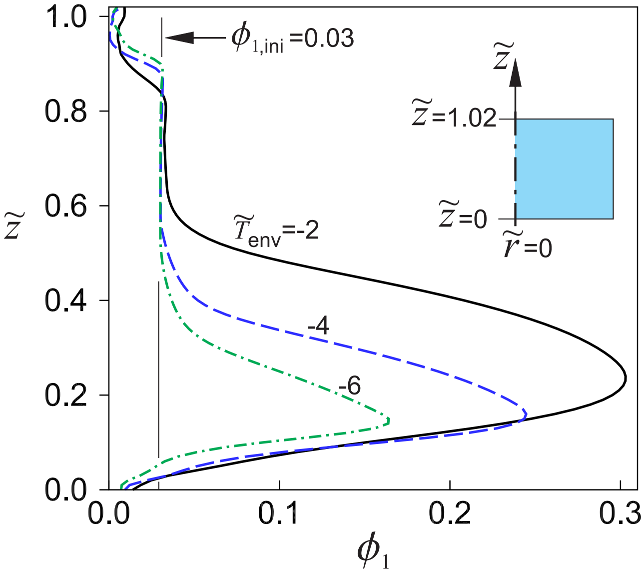

Fig. 12. Sucrose concentration ϕ_1 along the symmetric axis under different environmental temperatures: $\widetilde{T}_{\rm env} = -2$, -4, and -6.

solving one-dimensional Stefan problems [52] with a sharp moving interface. Second, the 3D axisymmetric thermal-fluid dynamics and mass transfer characteristics resulting from the phase-field model are presented in detail (Figs. 8–12), followed by a side-by-side comparison with experimental data (Fig. 13).

Formulations of the immobilized heat conduction equations and the boundary conditions for a moving interface are provided in Appendix A. This interfacial immobilization method essentially provides the sharp (zero thickness) interface limit to validate the phase-field approach with a thin but smooth and continuous interface. The axisymmetric system has only radial dependency so that the coordinate transformation can be carried out analytically.

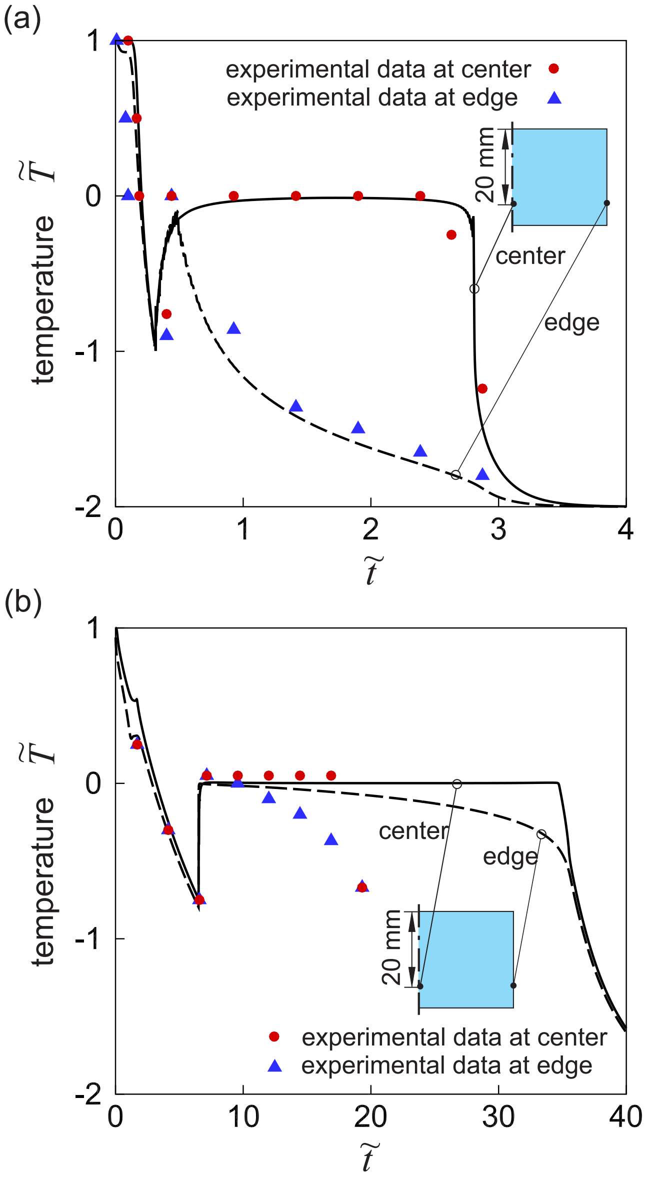

Fig. 13. Comparison of experimental results (data points) with the predicted temperature on the symmetric axis (solid line) and the circumferential side wall (dash line) during freezing of a pure water under (a) a fast cooling condition using liquid ethanol bath with approximated $h_{\rm top}$ and $h_{\rm side} \to \infty$, and (b) a natural convection with cold air surrounding the vessel. The configuration is delineated in Section 2.6 with $h_{\rm top} = 4.6$ W/(m$^2\cdot$K) and $h_{\rm side} = 7.9$ W/(m$^2\cdot$K) for case (b). The red dots indicate the experimental data on the symmetric axis and the blue triangles for the side wall. Both datasets are extracted from literature [15]. (For interpretation of the references to colour in this figure legend, the reader is referred to the web version of this article.)

Fig. 7 shows the computational results of freezing dynamics of pure water obtained from both methods. Finite difference schemes are applied to both approaches with a scaled time step 10^{-5} and 1000 uniform grid points along the radial direction. The thermophysical properties are phase dependent, and the heat transfer coefficient is set to $h = 7.9$ W/(m^{2}K) based on a natural convection condition given in Section 2.6. Fig. 7a–c are the transient results showing the location of the moving interface, temperature at the center point, and the moving velocity of the interface versus time. The initial condition is defined by a liquid phase with uniform temperature $\widetilde{T}_{\rm ini} = 1$ (283.15 K), and the ice phase grows progressively from the outer boundary ($\widetilde{b} = 1$) to the center point ($\widetilde{b} = 0$). The length and time scales are based on radius of the circular domain and the corresponding thermal diffusion time, $R_{\mathrm{i}} = 0.25$ cm, and $\tau_{\mathrm{T}} = 616.12$ s, respectively. Overall the phase-field approach agrees very well with the interface immobilization method at all transient steps. Specifically, the moving speed (scaled by $R_{\mathrm{i}}/\tau_{\mathrm{T}} \simeq 40.57$ μm/s) of the ice front ranges from 0 to about 6 μm/s, slightly increases as the ice phase just starts to develop and increases steeply as the front approaches to the center point. The relatively fast moving front is due to an efficient removal of the thermal energy while the front is moving to the center point and the phase transition area reduces significantly. The temperature profiles at several time instants are demonstrated in Fig. 7d, implying the corresponding temperature gradient and thus the strength of heat flux along the radial direction. Figure 7d has also demonstrated the temporal and spatial accuracy of the phase-field approach in both solid and liquid phases. The parameters used for interfacial energy, thickness, and mobility are feasible in simulating the macroscopic freezing dynamics. The maximum deviation of temperature between these two approaches is less than 0.05 K.

Fig. 8 shows computational results on cooling of water-sucrose-protein mixture (liquid phase only, before ice formation) in a cylindrical vessel. A sequence of images of temperature (top row) and mass density overlapped with velocity vectors (bottom row) are presented at scaled time instants $\tilde{t} = 0.5,\ 1.0,\ 1.2,\ 1.4$, and 2.0. The initial conditions include a uniform temperature $\tilde{T}_{\mathrm{ini}} = 1.0$ (283.15 K), uniform sucrose concentration $\phi_{1,\mathrm{ini}} = 0.03$, and protein concentration $\phi_{2,\mathrm{ini}} = 0.005$. The ambient temperature is fixed at $\tilde{T}_{\mathrm{env}} = -2.0$ (253.15 K) during the process. Several lumped heat transfer boundary conditions are provided in Section 2.6. Because the concentration of solutes remains uniform before ice starts to form, the local mass density of the liquid solution only varies with temperature. As shown in the sequential plots, near the beginning stage at time instant $\tilde{t} = 0.5$, the liquid solution near the circumferential side wall has lower temperature but higher density due to higher temperature gradient or stronger cooling effect coming from the wall boundary. The fluid flow driven by buoyancy (lower density at higher liquid temperature) results in a downstream flow sweeping through the side wall and circulating throughout the vessel. A lower temperature is observed at the lower part of the vessel at this point due to the downstream convective flow and also because that the bottom surface has a larger cooling effect comparing to the top surface. As the liquid solution continuously cools off, the highest density area appears at around temperature contour $\tilde{T} = 0.4$. From a closer look of the sequential plots one can observe the area with temperature $\tilde{T} < 0.4$ at $\tilde{t} = 1.0,\ 1.2$, and 1.4 is correlated with the decrease of density field. Overall the solution near the bottom and side walls has lower temperature and lower density than in the upper part of the vessel, which drives the fluid flow to a reverse direction from bottom back to the top. This motion enhances temperature uniformity and mixing of solutes within the vessel. Finally at $\tilde{t} = 2.0$, right before ice formation, the liquid solution is thermo-solutal stable with higher mass density near the bottom. The resulting flow reverses its direction only once in this case before ice formation. The circulation during this pre-ice formation period has velocity magnitude about 1.5×10^{-4} m/s.

Fig. 9 includes the transient dynamics in both liquid and solid phases, showing a long-time freezing process after ice starts to form. The transient results demonstrate the temperature distribution, location of ice/freeze-concentrate interface (or ice front), sucrose and protein concentrations in terms of volume fraction, and the velocity vectors of the fluid flow at time instants $\tilde{t} = 5,\ 15,\ 30$, and 33.8. The amount of supercooling and nucleation kinetics are neglected in this macroscopic model and the freezing temperature follows the equilibrium freezing temperature of a sucrose solution at various concentration. In this test case, sucrose has higher initial concentration 0.03 than the model protein 0.005, and thus the protein's contribution is assumed relatively small so that the correlations of temperature- and concentration-dependent thermophysical properties (except density that can be directly calculated) of the mixture are determined only by the sucrose content. Near the center point of the vessel, a thermal-arrest region (as also shown in Fig. 7b) is expected as the temperature in the liquid phase almost remains a value close to the equilibrium temperature. The temperature (top row) is in general lower near the side wall than at the top and bottom surfaces because of a stronger cooling effect from the side. As a result, the ice/freeze-concentrate interface (solid lines) appears first around the side wall, and then followed by a sporadic ice formation at top and bottom surfaces. The ice/freeze-concentrate interface approaches towards the center line from the top, bottom, and side walls after all surfaces are fully covered with ice at time around $\tilde{t} = 30$. The interface at $\tilde{t} = 33.8$ is developed to the upper center of the vessel due to higher cooling rate at the bottom comparing to the top surface, and the ice front moving velocity increases dramatically as the liquid phase is further confined to a smaller region in the middle of the vessel.

Furthermore, in Fig. 9, concentrations of sucrose and the model protein are illustrated in the middle and bottom rows, respectively. The freeze concentration effect appears in both cases, especially during the early stage of the freezing process as the slow moving ice front has a speed less than a micron per second, so that the system has sufficient time for solutes to be excluded from the ice phase. That is, the interfacial partition effect is near equilibrium. However, at the later stage as the moving speed of the ice front increases, the interfacial condition is no longer at equilibrium, and therefore solutes are largely left behind the interface and entrapped in the ice phase. Without more information about the microstructure and morphology of the ice crystals, this macroscopic prediction of non-equilibrium partition effect remains phenomenological. In the macroscopic process simulation, the freeze concentrate changes its local mass density on the liquid side of the solution, and thus its redistribution is further coupled with sedimentation and natural convection effects in the fluid flow. Near the beginning of ice formation at $\tilde{t} = 5$, both temperature and protein distributions are quite uniform, so that the downward flow only correlates with sucrose concentration, as a solute plume oberved in the figure. This indicates that the local flow instability is likely controlled by the segregated sucrose from sporadic patches of the ice phase initiated from the top surface. As the ice phase grows to $\tilde{t} = 15$ and 30, the overall concentration within the liquid domain increases more significantly, and the fluid flow becomes more stable due to less inertia in a confined region. Meanwhile, convection and sedimentation effects accumulate both types of solutes to the bottom portion of liquid phase, and the solute exclusion effect is weakened as ice front velocity increases. At $\tilde{t} = 33.8$, a significant amount of sucrose is left behind by a faster moving ice front, and entrapped by ice in the center/bottom portion of the vessel. The concentration of the model protein, however, shows accumulation at the top and bottom parts of the solution, and the effect is more significant along the symmetry axis. This is due to much larger molecular weight and an assumed smaller Flory's interaction parameter. For both types of solutes, local concentration varies significantly, but overall the center/bottom portion of the cylindrical vessel has more freeze concentrate introduced by the freezing process as expected from experimental observation [15].

Fig. 10 provides a closer look of the onset of flow instability near the top surface. The sequential plots show sucrose concentration and the velocity field at time instants around $\tilde{t} = 5$. The sporadic ice patches appeared at the top surface along with the freeze concentration effect increase local sucrose concentration, resulting in a Rayleigh-Taylor instability from the locally increased mass density. The higher concentration pocket of solution moves downward under the gravity effect, and the surrounding portion of the solution with lower concentration is displaced upward in this bounded domain. Later on the flow instability is weakened as sucrose diffuses into the bulk. Because the temperature field is quite uniform in the liquid solution during the freezing process, the Rayleigh-Bernard and double-diffusive instability can be neglected.

Fig. 11 shows temperature histories for specific locations along the symmetric axis and side wall in the vessel under different environmental temperatures. Following temperature contour maps shown in Figs. 8 and 9, the temperature distributions at these representative points for $\widetilde{T}_{\mathrm{env}} = -2$ (253.15 K) have only a small variation before the ice formation, and the uniform temperature distribution in the liquid phase is the signature of thermal-arrest phenomenon. The temperature uniformity is further enhanced by the convective effect. A closer look at the transient result, temperatures at 20 mm depth are slightly lower than the temperatures at 10 mm depth at the beginning of the process. This is simply due to a stronger cooling rate at the bottom than at the top surface. However, the same location at 20 mm depth has slightly higher temperature than at 10 mm as the direction of fluid flow reverses at about $\widetilde{T} \simeq 0.4$. The ice formation appears at about $\widetilde{t} = 2.2$. During freezing the temperature at the side wall gradually decreases due to strong heat flux out of the vessel, whereas the temperature along the symmetric line maintains its value near the equilibrium temperature T_{eq} (in a thermal-arrest region) until the ice front reaches the center part. During the freezing/exothermic process, the amount of latent heat that can be released relies on the temperature gradient established in the ice phase, which is influenced by the thermal resistance determined by the heat transfer boundary conditions. The time required to freeze the solution at 20 mm depth is shorter than that at 10 mm depth, revealing the trend of axial freezing direction from bottom to top in this test case that closely mimics the experimental conditions. At the final stage ($\widetilde{T}_{\mathrm{env}} = -2,\ \widetilde{t} > 34$), the temperatures at these locations are quite uniform because of higher thermal diffusivity in the ice phase, about 10^{-6} m^2/s, corresponding to lower characteristic thermal diffusion time about 570 s, than in the liquid phase (10^{-7} m^2/s, diffusion time about 4700 s). The temperature of the whole computational domain gradually decays to the ambient temperature at 253.15 K. The temperature profiles under different environmental settings are qualitatively similar. At a lower environmental temperature a steeper profile or stronger cooling rate leads to shorter cooling and freezing process time as expected. For the case of $\widetilde{T}_{\mathrm{env}} = -4$, the process time is about one half of the case $\widetilde{T}_{\mathrm{env}} = -2$ under the same heat transfer coefficient, and for $\widetilde{T}_{\mathrm{env}} = -6$, the processing time reduces to one third of the process time for $\widetilde{T}_{\mathrm{env}} = -2$. These results are consistent with a lumped approximation.

Following up test cases shown in Fig. 11, Fig. 12 further illustrates the corresponding sucrose concentration profiles ϕ_1 along the symmetric axis at the end of the freezing process. All of the results show significant accumulations of sucrose at the bottom/center part of the vessel due to sedimentation and buoyant effects, and solute partition at the ice/freeze concentrate interface as the ice front moves towards the inner region of the vessel. For the case $\widetilde{T}_{\mathrm{env}} = -2$, the maximum accumulated sucrose concentration, trapped in the ice phase near the center/bottom part of the vessel, is about ten times higher than its initial concentration (under the assumed kinetics model and coefficients proposed in eq. (40)). Because the partition effect is weaken as the moving speed of ice front increases, the location that has the highest solute concentration is not necessary the last point to freeze. That is, the freezing front may well enclose the freeze concentrate at higher moving speed. This is demonstrated on the sucrose concentration map in Fig. 9 at time instance at $\widetilde{t} = 33.8$. In case of lower environmental temperatures, stronger cooling leads to faster ice front velocity. The interfacial kinetics at a faster moving front results in less freeze concentration and thus a more uniform concentration profile, and in the end with maximum accumulation about five times higher than the initial value in this test case.

In Fig. 13 we compare the computational results with an excellent experimental study with relatively complete data and rigorous heat and mass transfer analysis developed by Rodrigues et al. [15]. The experiment used a 50 mL stainless steel vessel with 5 cm inner diameter and 7.5 mm wall thickness, covered by a 6 mm thickness lid. The vessel was cooled by either a circulating air (for a slow cooling) or liquid ethanol (fast cooling). The whole container was lifted up by three stoppers to avoid direct contact with the freezer. During the freezing process, temperature profiles were measured by thermocouples placed at various depths and radial locations within the vessel. The solute concentration was measured by UV spectroscopy on ice samples and assisted by protein staining for direct visualization. Measurements of solute concentration and the apparent freezing rate have uncertainty around 2 to 15%. Here we compare the computational results with experimental data for the pure water case within the vessel under fast (Fig. 13a) and slow (Fig. 13b) cooling conditions, in which the data points at 20 mm depth into the solution phase are extracted here for the validation. The initial temperature is set to $\widetilde{T}_{\mathrm{ini}} = 1$ (283.15 K), and the ambient temperature for both fast and slow cooling cases is $\widetilde{T}_{\mathrm{env}} = -2$ (253.15 K). For the fast cooling case (Fig. 13a) with vessel in a liquid ethanol bath we assume h_{top} and $h_{\mathrm{side}} \to \infty$, and the pure water is supercooled to about 263.15 K. Upon ice nucleation the temperature of the metastable liquid raises abruptly to the equilibrium freezing point around T_0 at time $\widetilde{t}$ about 0.3 (time scale 616 s). This is due to the fast release of latent heat. Without any fitting parameter, the numerical result very well predicts the cooling, temperature recovering, and freezing dynamics from the local measurements in experiments. The representative temperature on the side wall decreases quickly during the freezing process as ice starts to form, while the temperature on the symmetric axis maintains its value near freezing temperature in the thermal-arrest region until water at 20 mm depth is frozen. A good agreement is found between modeling and experimental results in terms of dynamic temperature distribution and characteristic time scales at each stages of the process under the fast cooling condition. Similarly, in Fig. 13b we compare the temperature profiles with experimental results under air cooling condition. The processing time is much longer due to smaller heat convection coefficients, estimated as $h_{\mathrm{top}} = 4.6$ $\mathrm{W}/(\mathrm{m}^2\cdot\mathrm{K})$ and $h_{\mathrm{side}} = 7.9$ $\mathrm{W}/(\mathrm{m}^2\cdot\mathrm{K})$ using the lumped resistance models. Both experimental and numerical results agree well in the cooling stage and show similar tendency as in the case under fast cooling condition. However, in the thermal arrest regime, our prediction on the process time is almost two times longer than the reported experimental observation. As a rough approximation using water properties one can estimate that the release of heat content during freezing of this amount of water is about five times longer than cooling under natural convection, which is consistent with the modeling result rather than the much shorter process time reported in experiment. Additional tests are suggested to clarify this contradiction during the freezing stage of a slow air cooling process.

5. Conclusion

A phase-field model is developed to describe the macroscopic freezing dynamics by coupling heat transfer, fluid flow, phase transition, interfacial kinetics and mass transfer of sucrose and model protein in a cylindrical vessel. The methodology agrees with the interface immobilization method often used in solving Stefan problems. The 3D axisymmetric results demonstrate the characteristic behaviors in freezing of water-sucrose-protein solutions particularly on the formation of freeze concentrate as the freezing front evolves during the process. Due to gravity effect, the thermosolutal contribution plays a significant role in temperature and concentration distributions, which are coupled with the evolution of ice/freeze-concentrate interface. Rayleigh-Taylor instability is observed briefly during the cooling/freezing process as several sporadic ice patches appeared at the top surface. The full process simulation including freeze concentration and thermal arrest behaviors are resolved by taking freezing point depression and temperature- and concentration-dependent properties into account. Although sucrose-protein association is neglected in this model, the multi-component mass transfer is demonstrated in this phase-field model including various degrees of solute exclusion across ice and liquid solution phases. A trapping of sucrose at the center/bottom part of the vessel and bipolarization distribution of a model protein are revealed in the test case. Overall the numerical results show good agreement with available experimental data except a contradictory point regarding the freezing process time under air cooling condition. The phase-field approach provides a great opportunity to model, investigate, predict, and design the freezing process for biopharmaceutical applications.

CRediT authorship contribution statement

Ji-Qin Li: Conceptualization, Methodology, Writing - original draft, Formal analysis, Visualization. **Tai-Hsi Fan:** Conceptualization, Methodology, Writing - review & editing, Supervision.

Acknowledgments

We acknowledge the financial supports of this research from the Kildsig Center for Pharmaceutical Processing Research (CPPR), and the National Science Foundation (CBET 1930906). We also thank B. Minatovicz, R. Bogner, S. Patel, L. Sun, and B. Chaudhuri for valuable feedback regarding freezing of biopharmaceuticals.

Appendix A. Interface immobilization method

In the quasi-1D approximation of phase change in a cylindrical configuration, the heat conduction equations in both liquid and solid domains can be formulated as

$$\frac{1}{\alpha_\ell}\frac{\partial T_\ell}{\partial t} = \frac{1}{r}\frac{\partial}{\partial r}\left(r\frac{\partial T_\ell}{\partial r}\right) \quad \text{for} \quad 0 \le r \le b(t), \tag{A.1}$$

and

$$\frac{1}{\alpha_s}\frac{\partial T_s}{\partial t} = \frac{1}{r}\frac{\partial}{\partial r}\left(r\frac{\partial T_s}{\partial r}\right) \quad \text{for} \quad b(t) \le r \le R_\mathrm{i}, \tag{A.2}$$

where α_s and α_ℓ are thermal diffusivities of solid and liquid phases, respectively, r is the radial coordinate, and the transient location of the solid-liquid interface at $r = b(t)$ is not known *a priori*, which needs to be determined as a part of the solution. The sharp interface boundary condition based on energy balance [52] is

$$k_s\frac{\partial T_s}{\partial r} - k_\ell\frac{\partial T_\ell}{\partial r} = \rho L_a\frac{db}{dt}, \tag{A.3}$$

where k_ℓ and k_s are thermal conductivities corresponding to the liquid and solid phases. All properties are constants in the test case, and the density for solid and liquid phase are the same in this simplified model. For the short-time cooling process, a liquid with a constant temperature T_ini is confined within the region $0 \le r \le R_\mathrm{i}$, where $r = 0$ indicates the symmetric axis and $r = R_\mathrm{i}$ has a convective boundary condition defined as

$$-k_\ell\frac{\partial T_\ell}{\partial r} = h(T - T_\mathrm{env}), \tag{A.4}$$

where h and T_env are the heat transfer coefficient and the environmental temperature. For the long-time freezing process, separated domains are applied to simulate the liquid and solid phases. The temperature at the interface $r = b(t)$ remains freezing temperature T_0 on both solid and liquid sides during the freezing process. Meanwhile, the temperature boundary condition on $r = R_\mathrm{i}$ becomes

$$-k_s\frac{\partial T_s}{\partial r} = h(T - T_\mathrm{env}). \tag{A.5}$$

The moving interface can be immobilized using a spatial coordinate transformation [53,54] in both liquid and solid domains as

$$\zeta = \frac{r}{b(t)} \quad \text{for} \quad 0 \le r \le b(t) \quad \text{and} \quad 0 \le \zeta \le 1, \tag{A.6}$$

and

$$\zeta = 1 + \frac{r - b(t)}{R_\mathrm{i} - b(t)} \quad \text{for} \quad b(t) \le r \le R_\mathrm{i} \quad \text{and} \quad 1 \le \zeta \le 2. \tag{A.7}$$

By defining characteristic temperature difference ΔT, length scale R_i, and time scale $\tau = R_\mathrm{i}^2/\alpha_s$, the corresponding scaled governing equations can be written as

$$\frac{\partial \widetilde{T}_\ell}{\partial \widetilde{t}} = \frac{\zeta}{\widetilde{b}}\frac{d\widetilde{b}}{d\widetilde{t}}\frac{\partial \widetilde{T}_\ell}{\partial \zeta} + \frac{\alpha_\ell/\alpha_s}{\widetilde{b}^2}\left(\frac{\partial^2 \widetilde{T}_\ell}{\partial \zeta^2} + \frac{1}{\zeta}\frac{\partial \widetilde{T}_\ell}{\partial \zeta}\right) \tag{A.8}$$

for $0 \le \zeta \le 1$,

$$\frac{\partial \widetilde{T}_s}{\partial \widetilde{t}} = \frac{2-\zeta}{1-\widetilde{b}}\frac{d\widetilde{b}}{d\widetilde{t}}\frac{\partial T_s}{\partial \zeta} + \frac{1}{(1-\widetilde{b})^2}\left(\frac{\partial^2 \widetilde{T}_s}{\partial \zeta^2} + \frac{1}{\zeta - 1 + \widetilde{b}/(1-\widetilde{b})}\frac{\partial \widetilde{T}_s}{\partial \zeta}\right) \tag{A.9}$$

for $1 \le \zeta \le 2$. And the interfacial boundary condition is

$$\frac{d\widetilde{b}}{d\widetilde{t}} = \mathcal{S}_\mathrm{te}\left(\frac{1}{1-\widetilde{b}}\frac{\partial \widetilde{T}_s}{\partial \zeta} - \frac{k_\ell/k_s}{\widetilde{b}}\frac{\partial \widetilde{T}_\ell}{\partial \zeta}\right) \tag{A.10}$$

at $\zeta = 1$, where the Stefan number $\mathcal{S}_\mathrm{te} = c_p\Delta T/L_a$. The corresponding boundary conditions in liquid phase are scaled as

$$\frac{\partial \widetilde{T}_\ell}{\partial \zeta} = 0 \quad \text{at} \quad \zeta = 0, \tag{A.11}$$

and

$$\frac{\partial \widetilde{T}_\ell}{\partial \zeta} = -\frac{k_s}{k_\ell}\mathcal{B}_\mathrm{i}(\widetilde{T} - \widetilde{T}_\mathrm{env}) \quad \text{at} \quad \zeta = 1, \tag{A.12}$$

during the cooling process, where the Biot number is defined as $\mathcal{B}_\mathrm{i} = hR_\mathrm{i}/k_s$. Whereas during the freezing process the boundary conditions are scaled as

$$\frac{\partial \widetilde{T}_\ell}{\partial \zeta} = 0 \quad \text{at} \quad \zeta = 0, \tag{A.13}$$

$$\widetilde{T}_\ell = \widetilde{T}_s = 0 \quad \text{at} \quad \zeta = 1, \tag{A.14}$$

and

$$\frac{\partial \widetilde{T}_s}{\partial \zeta} = -\mathcal{B}_\mathrm{i}(1-\widetilde{b})(\widetilde{T} - \widetilde{T}_\mathrm{env}) \quad \text{at} \quad \zeta = 2. \tag{A.15}$$

This method requires a time integration of the interface Eq. (A.10) to locate the transformed interfacial position $\widetilde{b}$.

References

[1] P.L. Privalov, Cold denaturation of proteins, Crit. Rev. Biochem. Mol. Biol. 25 (4) (1990) 281–305.

[2] B.S. Chang, B.S. Kendrick, J.F. Carpenter, Surface-induced denaturation of proteins during freezing and its inhibition by surfactants, J. Pharm. Sci. 85 (12) (1996) 1325–1330.

[3] G.B. Strambini, E. Gabellieri, Proteins in frozen solutions: evidence of ice-induced partial unfolding, Biophys. J. 70 (2) (1996) 971–976.

[4] M.C. Heller, J.F. Carpenter, T.W. Randolph, Manipulation of lyophilization-induced phase separation: implications for pharmaceutical proteins, Biotechnol. Prog. 13 (5) (1997) 590–596.
[5] K.-I. Izutsu, M.C. Heller, T.W. Randolph, J.F. Carpenter, Effect of salts and sugars on phase separation of polyvinylpyrrolidone-dextran solutions induced by freeze-concentration, J. Chem. Soc., Faraday Trans. 94 (3) (1998) 411–417.
[6] B.S. Bhatnagar, R.H. Bogner, M.J. Pikal, Protein stability during freezing: separation of stresses and mechanisms of protein stabilization, Pharm. Dev. Technol. 12 (2007) 505–523.
[7] B.S. Bhatnagar, M.J. Pikal, R.H. Bogner, Study of the individual contributions of ice formation and freeze-concentration on isothermal stability of lactate dehydrogenase during freezing, J. Pharm. Sci. 97 (2) (2008) 798–814.
[8] J.C. Kasper, W. Friess, The freezing step in lyophilization: physico-chemical fundamentals, freezing methods and consequences on process performance and quality attributes of biopharmaceuticals, Eur. J. Pharm. Biopharm. 78 (2011) 248–263.
[9] M.A. Miller, M.A. Rodrigues, M.A. Glass, S.K. Singh, K.P. Johnston, J.A. Maynard, Frozen-state storage stability of a monoclonal antibody: aggregation is impacted by freezing rate and solute distribution, J. Pharm. Sci. 102 (4) (2013) 1194–1208.
[10] A.K. Konstantinidis, W. Kuu, L. Otten, S.L. Nail, R.R. Sever, Controlled nucleation in freeze–drying: effects on pore size in the dried product layer, mass transfer resistance, and primary drying rate, J. Pharm. Sci. 100 (8) (2011) 3453–3470.
[11] D. Awotwe-Otoo, C. Agarabi, E.K. Read, S. Lute, K.A. Brorson, M.A. Khan, R.B. Shah, Impact of controlled ice nucleation on process performance and quality attributes of a lyophilized monoclonal antibody, Int. J. Pharm. 450 (2013) 70–78.
[12] S.S. Kulkarni, R. Suryanarayanan, J.V. Rinella Jr., R.H. Bogner, Mechanisms by which crystalline mannitol improves the reconstitution time of high concentration lyophilized protein formulations, Eur. J. Pharm. Biopharm. 131 (2018) 70–81.
[13] , Lyophilization of Pharmaceuticals and Biologicals: New Technologies and Approaches, K.R. Ward, P. Matejtschuk (Eds.), Humana Press, New York, 2019.
[14] M.F. Butler, Freeze concentration of solutes at the ice/solution interface studied by optical interferometry, Cryst. Growth Des. 2 (6) (2002) 541–548.
[15] M.A. Rodrigues, M.A. Miller, M.A. Glass, S.K. Singh, K.P. Johnston, Effect of freezing rate and dendritic ice formation on concentration profiles of proteins frozen in cylindrical vessels, J. Pharm. Sci. 100 (4) (2011) 1316–1329.
[16] S.K. Singh, P. Kolhe, A.P. Mehta, S.C. Chico, A.L. Lary, M. Huang, Frozen state storage instability of a monoclonal antibody: aggregation as a consequence of trehalose crystallization and protein unfolding, Pharm. Res. 28 (2011) 873–885.
[17] J.C. Kasper, M.J. Pikal, W. Friess, J. Pharm, Investigations on polyplex stability during the freezing step of lyophilization using controlled ice nucleation - the importance of residence time in the low-viscosity fluid state, J. Pharm. Sci. 102 (3) (2013) 929–946.
[18] M.A. Rodrigues, G. Balzan, M. Rosa, D. Gomes, E.G. de Azevedo, S.K. Singh, H.A. Matos, V. Geraldes, The importance of heat flow direction for reproducible and homogeneous freezing of bulk protein solutions, Biotechnol. Prog. 29 (5) (2013) 1212–1221.
[19] T.-H. Fan, J.-Q. Li, B. Minatovicz, E. Soha, L. Sun, S. Patel, B. Chaudhuri, R. Bogner, Phase-field modeling of freeze concentration of protein solutions, Polymers 11 (2019) 10.
[20] R.G.M. van der Sman, Phase field simulation of ice crystal growth in sugar solutions, Int. J. Heat Mass Transf. 95 (2016) 153–161.
[21] M. Brülls, A. Rasmuson, Heat transfer in vial lyophilization, Int. J. Pharm. 246 (2002) 1–16.
[22] N. Radmanovic, T. Serno, S. Joerg, O. Germershaus, Understanding the freezing of biopharmaceuticals: first-principle modeling of the process and evaluation of its effect on product quality, J. Pharm. Sci. 102 (8) (2013) 2495–2507.
[23] F.G.F. Qin, J.C. Zhao, A.B. Russell, X.D. Chen, J.J. Chen, L. Robertson, Simulation and experiment of the unsteady heat transport in the onset time of nucleation and crystallization of ice from the subcooled solution, Int. J. Heat Mass Transf. 46 (2003) 3221–3231.
[24] K. Nakagawa, A. Hottot, S. Vessot, J. Andrieu, Modeling of freezing step during freeze-drying of drugs in vials, AIChE J. 53 (5) (2007) 1362–1372.
[25] C.R. Muzzio, N.G. Dini, Simulation of freezing step in vial lyophilization using finite element method, Comput. Chem. Eng. 35 (2011) 2274–2283.
[26] U. Roessl, D. Jajcevic, S. Leitgeb, J.G. Khinast, B. Nidetzky, Characterization of a laboratory-scale container for freezing protein solutions with detailed evaluation of a freezing process simulation, J. Pharm. Sci. 103 (2014) 417–426.
[27] H. Emmerich, The Diffuse Interface Approach in Materials Science: Thermodynamic Concepts and Applications of Phase-Field Models, Springer, Berlin, 2003.
[28] J.W. Cahn, J.E. Hilliard, Free energy of a nonuniform system. I. Interfacial free energy, J. Chem. Phys. 28 (1958) 258–267.
[29] P.C. Hohenberg, B.I. Halperin, Theory of dynamic critical phenomena, Rev. Mod. Phys. 49 (3) (1977) 435–479.
[30] O. Penrose, P.C. Fife, Thermodynamically consistent models of phase-field type for the kinetics of phase transitions, Physica D 43 (1990) 44–62.
[31] S.-L. Wang, R.F. Sekerka, A.A. Wheeler, B.T. Murray, S.R. Coriell, R.J. Braun, G.B. McFadden, Thermodynamically-consistent phase-field models for solidification, Physica D 69 (1993) 189–200.
[32] R. Kobayashi, Modeling and numerical simulations of dendritic crystal growth, Physica D 63 (1993) 410–423.
[33] J. A. Warren, W.J. Boettinger, Prediction of dendritic growth and microsegregation patterns in a binary alloy using the phase-field method, Acta Metall. Mater. 43 (2) (1995) 689–703.
[34] B.T. Murray, A.A. Wheeler, M.E. Glicksman, Simulations of experimentally observed dendritic growth behavior using a phase-field model, J. Cryst. Growth 154 (1995) 386–400.
[35] A. Karma, W.J. Rappel, Phase-field method for computationally efficient modeling of solidification with arbitrary interface kinetics, Phys. Rev. E 53 (4) (1996) R3017–R3020.
[36] A. Karma, W.J. Rappel, Quantitative phase-field modeling of dendritic growth in two and three dimensions, Phys. Rev. E 57 (4) (1998) 4323–4349.
[37] C. Beckermann, H.-J. Diepers, I. Steinbach, A. Karma, X. Tong, Modeling melt convection in phase-field simulations of solidification, J. Comput. Phys. 154 (1999) 468–496.
[38] W.J. Boettinger, J.A. Warren, C. Beckermann, A. Karma, Phase-field simulation of solidification, Annu. Rev. Mater. Res. 32 (2002) 163–194.
[39] D.M. Anderson, G.B. McFadden, A.A. Wheeler, Diffuse-interface methods in fluid mechanics, Annu. Rev. Fluid Mech. 30 (1998) 139–165.
[40] D.M. Anderson, G.B. McFadden, A.A. Wheeler, A phase-field model of solidification with convection, Physica D 135 (2000) 175–194.
[41] Z. Bi, R.F. Sekerka, Phase-field model of solidification of a binary alloy, Physica A 261 (1998) 95–106.
[42] J.-Q. Li, T.-H. Fan, T. Taniguchi, B. Zhang, Phase-field modeling on laser melting of a metallic powder, Int. J. Heat Mass Transf. 117 (2018) 412–424.
[43] J.-Q. Li, T.-H. Fan, Phase-field modeling of metallic powder-substrate interaction in laser melting process, Int. J. Heat Mass Transf. 133 (2019) 872–884.
[44] S. Mondal, M. Phukan, A. Ghatak, Estimation of solid–liquid interfacial tension using curved surface of a soft solid, Proc. Natl. Acad. Sci. U.S.A. 112 (2015) 12563–12568.
[45] T.L. Bergman, F.P. Incropera, D.P. DeWitt, A.S. Lavine, Fundamentals of Heat and Mass Transfer, John Wiley & Sons, New York, 2011.
[46] W.M. Lewandowski, P. Kubski, J.M. Khubeiz, Natural convection heat transfer from round horizontal plate, Wärme- und Stoffübertragung 27 (1992) 281–287.
[47] , CRC Handbook of Chemistry and Physics, D.R. Lide (Ed.), CRC Press, Boca Raton, FL, 2004.
[48] A. Dehaoui, B. Issenmann, F. Caupin, Viscosity of deeply supercooled water and its coupling to molecular diffusion, PNAS 112 (39) (2015) 12020–12025.
[49] J.F. Swindells, C.F. Snyder, R.C. Hardy, P.E. Golden, Viscosities of sucrose solutions at various temperatures: tables of recalculated values, NBS Circular 440 (1958).
[50] , The Plasma Proteins: Structure, Function, and Genetic Control, F.W. Putnam (Ed.), Academic Press, New York, 1975.
[51] F.E. Young, F.T. Jones, Sucrose hydrates. the sucrose-water phase diagram, J. Phys. Chem. 53 (1949) 1334–1350.
[52] M.N. Özisik, Heat Conduction, John Wiley & Sons, New York, 1993.
[53] T.-H. Fan, F.B. Cheung, Modeling of transient turbulent natural convection in a melt layer with solidification, J. Heat Transf. 119 (1997) 544–552.
[54] H. Song, C.-R. He, C. Basdeo, J.-Q. Li, D. Ye, D. Kalonia, S.-Y. Li, T.-H. Fan, Evaporation of binary mixtures and precision measurement by crystal resonator, Int. J. Heat Mass Transf. 100 (2016) 800–809.